

**A computational study of turbulent separated flow  
over a wall mounted cube at two different Reynolds  
numbers and incoming velocity profiles**

---

*Technical Report*

Computational Science Division

## **CPS Technical Report**

CPS Technical Reports are one or more of the following: documentation of scientific code developments, project reports, workshop reports, papers submitted to conferences, papers submitted to journals, and other presentation material.

## **About Argonne National Laboratory**

Argonne is a U.S. Department of Energy laboratory managed by UChicago Argonne, LLC under contract DE-AC02-06CH11357. The Laboratory's main facility is outside Chicago, at 9700 South Cass Avenue, Argonne, Illinois 60439. For information about Argonne and its pioneering science and technology programs, see [www.anl.gov](http://www.anl.gov).

## **DOCUMENT AVAILABILITY**

**Online Access:** U.S. Department of Energy (DOE) reports produced after 1991 and a growing number of pre-1991 documents are available free at OSTI.GOV (<http://www.osti.gov/>), a service of the U.S. Dept. of Energy's Office of Scientific and Technical Information

### **Reports not in digital format may be purchased by the public from the National Technical Information Service (NTIS):**

U.S. Department of Commerce  
National Technical Information Service  
5301 Shawnee Rd  
Alexandria, VA 22312  
**[www.ntis.gov](http://www.ntis.gov)**  
Phone: (800) 553-NTIS (6847) or (703)  
605-6000 Fax: (703) 605-6900  
Email: **[orders@ntis.gov](mailto:orders@ntis.gov)**

### **Reports not in digital format are available to DOE and DOE contractors from the Office of Scientific and Technical Information (OSTI):**

U.S. Department of Energy  
Office of Scientific and Technical Information  
P.O. Box 62  
Oak Ridge, TN 37831-0062  
**[www.osti.gov](http://www.osti.gov)**  
Phone: (865) 576-8401  
Fax: (865) 576-5728  
Email: **[reports@osti.gov](mailto:reports@osti.gov)**

## **Disclaimer**

This report was prepared as an account of work sponsored by an agency of the United States Government. Neither the United States Government nor any agency thereof, nor UChicago Argonne, LLC, nor any of their employees or officers, makes any warranty, express or implied, or assumes any legal liability or responsibility for the accuracy, completeness, or usefulness of any information, apparatus, product, or process disclosed, or represents that its use would not infringe privately owned rights. Reference herein to any specific commercial product, process, or service by trade name, trademark, manufacturer, or otherwise, does not necessarily constitute or imply its endorsement, recommendation, or favoring by the United States Government or any agency thereof. The views and opinions of document authors expressed herein do not necessarily state or reflect those of the United States Government or any agency thereof, Argonne National Laboratory, or UChicago Argonne, LLC.

# **A computational study of turbulent separated flow over a wall mounted cube at two different Reynolds numbers and incoming velocity profiles**

---

*Technical Report*

Computational Science Division

prepared by  
Sigfried Haering, Ramesh Balakrishnan and Rao Kotamarthi

July 27, 2021

# A computational study of turbulent separated flow over a wall mounted cube at two different Reynolds numbers and incoming velocity profiles

S. Haering<sup>\*1</sup>, R. Balakrishnan<sup>†1</sup>, and V. R. Kotamarthi<sup>‡2</sup>

<sup>1</sup> Computational Science Division, Argonne National Laboratory, Argonne, IL

<sup>2</sup> Environmental Science Division, Argonne National Laboratory, Argonne, IL

## Abstract

Simulations of the canonical wall-mounted unit cube subjected to two distinct incident velocity profiles is performed at Reynolds numbers ( $Re$ ) where the bulk flow characteristics are known to become relatively  $Re$ -insensitive using both direct numerical simulation (DNS) and wall-resolved large eddy simulation (WRLES). The aim of this work is to highlight the sensitivity of such bluff-body flows to mean shear and to provide a representative set of data for such flow scenarios where common turbulence modeling techniques often fail. Simple boundary conditions are selected to allow for easy comparisons for model development purposes and avoid confounding effects from freestream turbulence. In addition to mean velocity profiles, select turbulence statistics are presented in detail. We find that both mean velocity profiles and mean wake turbulence are  $Re$ -insensitive over the range examined here.

## 1 Introduction

The case of the wall-mounted cube (WMC) in crossflow and its variants have been of interest to multiple engineering communities for well over 50 years. High Reynolds number ( $\mathcal{O} \sim 10^7$ ) WMC studies take on the basic characteristics of wind flow around buildings and urban settings and is thus of interest in city planning, pollution dispersement, and distributed wind energy [1–6]. Mid-range Reynolds number WMC ( $\mathcal{O} \sim 10^5$ ) are useful for examining aerodynamic drag and noise around bluff bodies commonly occurring in automotive and train freight [7–10]. Low Reynolds number WMC-like flows have more recently seen interest related to convectively cooled cubic micro devices to improve performance and longevity of integrated circuitry [11, 12]. From the perspective of a basic roughness element, arrays of simple cube-like objects have seen extensive interest [13–20], due to their wide range of applicability from the study of drag, for instance over riveted ship hulls, to urban atmospheric boundary layers.

While these flows are related by the fundamental structure of the obstacles, actual flow conditions vary widely beyond just the Reynolds number considerations. As identified in [21], the main properties affecting these flow types are the obstacle geometry, incident boundary layer thickness, freestream turbulence, wall shear stress, and angle-of-attack. Each of these considerations impact the basic flow features in different ways. For instance, the obstacle aspect ratio will cause the fundamental flow structure to

---

<sup>\*</sup>shaering@anl.gov

<sup>†</sup>bramesh@anl.gov

<sup>‡</sup>vrkotamarthi@anl.gov

transition from the classic three-dimensional separation bubble to a quasi-two-dimensional more fence-like structure with increasing spanwise aspect ratio, to a backward-facing step as both the streamwise and spanwise aspect ratios increase, to a square-cylinder type flow with only the vertical aspect ratio increasing. Such transitions are due to the degree of flow reattachment on the obstacle roof and the majority of free stream momentum being forced over the sides or the top of the obstacle as opposed to around all sides and have significant effects of the obstacle flow and wake recovery. Obstacles may be deeply immersed in a boundary layer and therefore subjected to strong mean shear profiles. Bluff-body flows are naturally sensitive to incident flow profiles and mean gradients. Due to elevation-dependent momentum flowing around the obstacle, the resulting wake and recirculation region shape will be distorted accordingly. Additionally, due to sustained turbulent production through the interactions of the obstacle-induced-turbulence and the mean strain, incoming boundary layer thickness can be expected to have significant effects on the decay of wake turbulence. Free stream turbulence intensity will vary greatly from application-to-application or even within a single application. For instance, building and city level atmospheric turbulence varies greatly with seasons and even throughout the diurnal cycle. Such changes can be expected to affect the turbulent production in the thin shear layers very near to the obstacle surface. While the incident flow can be selected or is constant for some applications, e.g. micro device cooling applications, we have no such control for buildings resulting in a large ensemble of orientations and potential flow properties and wakes. Thus, there is a need to study the WMC-type flows in a variety of, and potentially very specific, test conditions.

As a result of the broad application and numerous flow sensitivities, wall-mounted bluff bodies have indeed seen extensive study. Nonetheless, open questions still remain. Often, the recirculation and wake behavior are thought to be largely Reynolds number independent at moderate  $Re$  [22–24]. However, this is may be only true for oblique incoming flow. With a sharp leading-edge, the forward stagnation is inherently unstable and the size of delta-wing vortex formed around the sides of such non-oblique bluff-body flows is dictated by the viscous dissipation at its core leading lead to Reynolds number sensitivity [25]. Another potential issue is the effects of stratification and stability on an obstacle wake which has, to date, only been examined for a very small number of obstacle shapes and conditions [26–28]. Actual field conditions are very difficult to simulate in a wind tunnel and impossible to perform numerically, without significant modeling, due to the computational costs. Conflicting requirements of high  $Re$  and large boundary layer thicknesses (relative to the cube dimension), varying stability and free stream turbulence make experiments of such flows very challenging. Only recently [29], have near-atmospheric stability conditions been achieved in wind tunnels. Naturally, such flow parameters have confounding effects, making direct application of information drawn from experiments and simulations problematic in practice.

While specific applications of wall-mounted obstacle flows are certainly plentiful, perhaps the more useful impact of their study stems from their generally rich flow morphology due to their potential broad-reaching application. That is, being comprised of many “building-block” features, the basic flow itself may be useful for both validation and development of turbulence models beyond the information available from canonical flows with one and two-dimensional means. Flow separation, smooth-wall reattachment, transition, adverse and favorable pressure gradients, and three-dimensional wall bounded turbulence are all inherent to the WMC and are all known to cause difficulties with RANS and subgrid scale (SGS) models. While wake velocity profiles have been demonstrated to be Reynolds number independent for oblique inflows from  $Re_h \approx 3000$  [22–24] or, at most,  $Re_h \approx 20K$  [25], flows at different  $Re_h$  are still of prime interest for model development purposes. It is this bulk flow insensitivity to  $Re_h$  that contributes to utility of the WMC for this purpose. As  $Re$  is increased, the only way for the separation region to remain unaffected is for the momentum transport terms to exactly balance the increasing inertial forces. If turbulent momentum transport is significant to the wake dynamics, the wake turbulence must then be

strongly  $Re$ -dependent. On the other hand, the wake may be primarily a result of the balance between inertial and pressure forces. In this case, the increasing turbulent production around the cube resulting from the increased  $Re$  must be balanced by increased turbulent dissipation. Maintaining this balance is challenging for turbulence models. In the context of RANS, a successful model may need to be able to predict both the increasing turbulent production and the highly three-dimensional and anisotropic momentum transport across the separated shear layer and recirculation bubble. Such difficulties, along with well-documented limitation of linear eddy viscosity models [30, 31], have motivated the addition of nonlinear terms [32] not of the eddy viscosity form to improve wake prediction. While certainly encouraging, more work in this direction is warranted. Further, the high  $Re$  WMC-like simulations for building and wind applications precludes wall-resolved simulation and necessitates use of wall functions (RANS) or wall models (LES). However, with the exception of wall models which rely on separate wall-resolved simulations [33], functions and models make strong assumptions about the condition of the unresolved flow such as local equilibrium or law-of-the-wall unresolved profiles [34]. While dubious when applied in the near-cube recirculation region, such models would be wildly incorrect if applied to the actual cube surface and cube-edges. Information gleaned from WMC simulations may lead to improved and robust wall modeling in general.

The work performed here is intended to provide high-fidelity simulation data of a WMC and its near wake subjected to two different incident velocity profiles and no free stream turbulence. The problem conditions simulated do not directly correspond to any physical system; the geometry is small and boundary conditions are idealized. However, it is precisely these simplifications that make the case useful for the purpose of model evaluation and development. The domain is small enough to be computationally tractable while being large enough to fully encompass all the most critical near-cube and wake features. The inflow conditions are easily reproducible and do not require generation of synthetic turbulence. For LES, generation of resolved free stream turbulence is particularly difficult with a number of different methods used [35]. Simple inflow conditions obviate the additional ad-hoc simulation complexities of prescribing synthetic turbulence and associated potential long domains necessary for “healing” of the inflow. Statistics from computational-simple yet feature-rich simulations, such as Reynolds stress, production, and dissipation are highly desirable. Though the work presented here is not in and of itself novel or illuminating, it is the hope of the authors that the simplicity of the cases will make this data of use for improving RANS and SGS models as well as highlighting the effects of mean velocity gradients on wake characteristics.

This paper is organized as follows. Section 2 presents a brief, and by no means exhaustive, overview of the vast amount of related work performed to date. Simulation conditions and simulation quality assessment are presented in Section 3. Results with a focus on turbulence statistics potentially useful for model development and comparisons between the different inflows and  $Re$  are presented in Section 4. Finally, concluding statements are provided in Section 5.

## 2 Background

There has been an extensive amount of experimental and numerical work performed on wall-mounted bluff bodies. Though the body of work is nearly exhaustive, additional details useful to improve turbulence modeling remain useful. As previously discussed, this need is more a result of the difficulty in reproducing wind-tunnel experimental conditions in a simulation as opposed to the number of experiments performed with available data. Here, we recount significant experiments and simulations and their main findings. For a more complete list of works related to obstacle flows in wind engineering, the reader is referred to the reviews [1–4, 36], amongst others.

Early experimental work performed by Castro and Robins [37] for a WMC at  $Re_h \approx 4000$  showed that the upstream turbulence and mean shear has a strong effect on reducing the size of separation regions and reducing wake recovery distances. In their study, boundary layer thicknesses of  $\delta_{99}/h = 0.0375$  and 10 were considered. The nearly-uniform case was accompanied by a small amount of free stream turbulence intensity (0.5%) while the thick boundary case contained a varying and high level of nearly 20% at the cube height. For both cases, the wake recovered to nearly the incident flow by 4.5 downstream of the cube. However, by  $2h$  downstream, the thick boundary layer wake had fully reattached whereas the recirculation bubble for uniform inflow was still present. Profiles of mean velocity and turbulence intensity are provided at multiple downstream locations. With the large difference in boundary layer turbulence of the two cases, it is difficult to separate the effects of the mean shear from the free stream turbulence. The more recent experimental work of Hearst *et.al.* [38] has revealed the effects of freestream turbulence to be minimal. Over a range of freestream turbulence intensity from approximately 4% to 10%, they observe only a few percent decrease in wake recirculation length which also appeared to saturate before the final intensity level probed. However, a single turbulence generation method was used for all experiments so that it cannot be ruled out that different energy-containing scales would cause different wake effects. Additionally, the freestream turbulence length scale has been shown to have a significant effect on pressure fluctuations and reattachment from the leading edge of a bluff body [39]. Nonetheless, it appears mean shear is the dominate contribution to the differences observed in [37].

The effects of spanwise aspect ratio on the wake were examined by Martinuzzi and Tropea [21] at  $Re_h \approx 40K$ . Increasing the aspect ratio results in asymptotic approach to a maximum reattachment length of  $7h$  downstream of the obstacle. From aspect ratios of 1 to 5, the reattachment length increases linearly from the standard unit cube value of approximately  $1.6h$  to  $5h$  with a shift to a much more gradual extension of the wake length with increasing aspect ratio. However, the pressure coefficient leading up to the obstacle was found to continually increase with aspect ratio and similarly decrease in the recirculation region without any saturation behavior observed up to the highest aspect ratio examined of 24.

The effects of angle of attack were also probed in [37] where an angle of  $45^\circ$  was examined for both inflow conditions. They observed very little effect for the thick boundary layer case but a smaller, elevation-wise, wake recirculation bubble that reattached at the same location. Additionally, wake turbulence intensities were decreases for the latter case while again begin relatively insensitive for the former. Sand erosion visualization techniques [40] have revealed an elongation of the wake recirculation region by approximately  $2\times$  with increased reverse flow speeds at wind angles of  $30^\circ$  and obstacles of aspect ratios of 2.

The complexity of WMC flow structure is highlighted by many detailed discussions of the oscillating vortex shedding and stationary vortex system generated around three-dimensional wall-mounted obstacles [21, 36, 37, 41–43]. In the  $Re$ -independent regime, Schofield and Logan [36] argue for a total of eight major vortices, including multiple upstream-originating horseshoe vortices, a “roof” vortex, and three distinct separation vortices. Others [37, 41] have shown multiple vortex formation on the cube roof. Many wall-pattern flow visualizations have been used towards this end as well [42, 44]. While being of prime interest for particular engineering applications and useful for model validation, such information is not useful for model development as they provide no turbulence details. In addition to experiments which provide Reynolds stress information, highly-resolved numerical simulations have provided critical statistics.

Though over 20 years old, the findings of the bluff-body CFD workshop of Rodi *et.al.* [24] are still relevant today. In their comparisons of multiple simulations from various research groups of the WMC of [21]

in a fully developed channel of height  $2h$  at  $Re_h = 40K$ , they came to three conclusions. First, while “law of the wall” models for LES boundary conditions do reduce simulation by an order of magnitude, they are not reliable for these type of flows. The more recent study of Lim *et.al.* [25] showed more advanced wall models are capable of capturing general flow features but poorly predict turbulence levels for flow around a cube. However, wall-resolved LES has been shown to perform well [45]. Second, time averaging for over 100 convective times (based on  $h$ ) is not sufficient for even linear statistics (*i.e*  $\langle u \rangle$ ) to converge with asymmetries in the wake profiles clearly visible in all LES simulations. Finally, multiple unsteady Reynolds-averaged Navier-Stokes (RANS) models over predict the reattachment length of  $1.6h$  by 60-70%. Subgrid models considered included the basic Smagorinsky [46], dynamic Smagorinsky [47], and Schumann [48] while RANS models used basic  $k-\varepsilon$  [49], Kato-Launder (KL)  $k-\varepsilon$  [50], and KL with a two-layer approach [51].

It is generally accepted that unsteady vortex shedding makes steady RANS simulations insufficient for the prediction of bluff-body flows. However, the failures of multiple unsteady RANS (URANS) simulations in the aforementioned CFD workshop suggests additional model refinements are necessary. The trend of unsteady RANS models delaying reattachment was also seen in the study of Ratnam *et.al.* [52] using various forms of the  $k-\varepsilon$  and  $k-\omega$  model at  $Re_h = 1870$  with a fully developed channel of  $3h$ . In comparison with the DNS of Yakhot *et.al.* [23], reattachment lengths were again over predicted the expected value of  $1.5h$  by as much as 55%. The non-linear  $k-\varepsilon$  model [32] performed the best with only a 30% over prediction. However, an improved  $k-\omega$  model [53] provided the best estimate of the forward separation, off by  $< 10\%$ , and accurately reproduced the cube-top recirculation. Both models were found to under predict the the  $\langle u'v' \rangle$  shear stress component by approximately 50% in the detached shear layer along the center of the cube from above the trailing edge of the cube to about  $1h$  downstream. This detailed comparison suggests the main reason for RANS models failing to predict the correct reattachment length around bluff body flows is insufficient cross-shear layer turbulent momentum transfer just aft of the obstacle. Improvements with a non-linear  $k-\varepsilon$  model were shown at a higher  $Re_h$  of  $5 \times 10^4$  in a fully developed channel of  $2h$  [32]. In comparison with the experiments of Larousse *et.al.* [54], one of their proposed “non-linear” models nearly reproduced the reattachment point of  $1.5h$  with only a small delay of about 17% as well as better reproducing the turbulent kinetic energy around the cube surface. Elliptic relaxation models accounting for near-wall effects [55] have shown similar improvements with only a 16% delay of reattachment [56]. This appears to be best performing RANS model in the literature.

Due to computational cost, few actual DNS have been performed of the WMC geometry. Low  $Re_h$  studies ( $\leq 1500$ ) have been performed by [57] but, as the flows do not become significantly turbulent, they are not of interest to this work. DNS by Diaz-Daniel *et.al.* [58] examined a range of WMC from  $Re = 550$  to 3000 using a laminar Blasius inflow of  $\delta_{99} = 1h$  and a turbulent boundary layer of  $2.4h$ . A large domain of  $320 \times 27 \times 10h$  and over 500M grid points were used making the study ideal for extracting a large amount of high-quality data. However, the study focused on the power spectra of the dynamic structures generated by the cube and little wake or turbulence statistics are provided. A “tall cube” with aspect ratio 4 was simulated been by Saedi *et.al.* [59] at  $Re_b = 12K$  where  $b$  indicates the base width. The building-like obstacle was subjected to an incident turbulent boundary layer of  $\delta_{99} = 0.18h$ . Over 35M grid points were used with a second-order staggered finite difference code so that the ratio of the grid to Kolmogorov scale,  $\eta$ , was all order unity with an average of  $\approx 5$  in the wake region. Detailed wake velocity, Reynolds stress and turbulent production profiles are provided and results are shown to be in excellent agreement with wind tunnel experiments of [60] and [61]. Vinuesa *et.al.* [62] also examined the case of a “tall cube” with aspect ratio 4 subjected to a laminar and turbulent inflow of  $Re_\theta \approx 1K$ . No assessment of the simulation quality is presented however, mean wake velocity profiles are in reasonable agreement with [60]. Additional wake turbulence intensities are provided. Despite the

different simulations and inflow conditions considered, the reattachment point for both [62] and [59] was nearly the same at  $\approx 3.7h$  downstream of the obstacle.

The most similar DNS to the work presented here is the aforementioned work of Yakhot *et.al.* [23] performed at  $Re_h = 1870$  using the immersed boundary method. A computational domain of  $14h \times 3h \times 6.4h$  and 5M grid points resulted in the majority ( $> 90\%$ ) of grid to Kolmogorov scale ratios being less than six. While larger than the fully-resolved DNS ratio of  $\sim 1.5$  [63], the authors believe calculated Kolmogorov length scales are conservatively small due to local anisotropy. The numerical method was a second-order staggered formulation with no-slip of the cube enforced through immersed boundary forcing as suggested by Kim *et.al.* [64]. However, while the grid was clustered in the wall normal direction near the channel walls, it seems the same clustering was not performed at the cube surface. Without cube surface grid refinement, near-surface flow features at the cube, such as production and reattachment, are questionable. The inlet condition made use of an auxiliary fully developed channel flow simulation. While certainly closer to common experiments, it is not convenient for the purposes of model development. Nonetheless, the reported data for turbulent kinetic energy, Reynolds stress, and dissipation are invaluable for model development.

### 3 Simulation conditions

Characteristics of the flows of interest for this study include a bluff body subjected to some non-uniform incident velocity profile to create a region of massive separation and recirculation followed by a wake with a recovering velocity deficit. We must balance these requirements with the large computational burden of a proper DNS. To satisfy these requirements, we have performed a small, yet feature rich, true DNS at a Reynolds number, 3900 based on the cube height, where much of the flow characteristics have been observed to become largely  $Re$ -independent [22–24]. Lim *et.al.* [25] argue  $Re$ -insensitivity does not occur until  $Re_h = 20K$ . Comparison with DNS at  $Re_h = 3900$  and WRLES at  $Re_h = 20K$  is performed to examine bulk flow difference between this  $Re$  range. Further, the simulation domain is extended for the WRLES to examine inflow effects on the far wake. Naturally, the different simulation domains of the two cases makes any direct comparison of the two simulation  $Re$  only qualitative. In addition to mean velocity profiles, Reynolds stress, dissipation, and production statistics are gathered to aid in the evaluation and potential development of SGS and RANS models. To ensure a true DNS, both the ratios of the Kolmogorov length scale to every grid direction and the wall-normal grid spacing are evaluated.

Details for the simulation are as follows. For the DNS, a uniform cube of dimension  $1h$  is mounted to a smooth non-slip surface in a box of size  $(7.5 \times 3.0 \times 2.0)h$  with a wake length of  $4.5h$ . The higher  $Re$  domain is extended to  $(25 \times 10.0 \times 5.0)h$  with a wake length of  $19.5h$ . Throughout this paper, the streamwise direction will be referred to as the  $x$ -direction, the “ground” normal as the  $y$ -direction, and the spanwise direction as the  $z$ -direction. Unless otherwise specified, the coordinate system is centered about the base of the cube so that the cube itself extends from  $(-0.5:0.5)$  in  $x$ ,  $(0:1)$  in  $y$ , and  $(-0.5:0.5)$  in  $z$ . Periodic boundary conditions are used on side boundaries and a slip condition is applied at the top of the domain. Periodicity effectively simulates a series of cubes with a gap of  $2h$ . The slip condition is not representative of an obstacle in a channel, much less the atmospheric boundary layer, and more closely represents simulation of a flat plate instead of a fully developed channel.

Two laminar inflow conditions are considered: Blasius boundary layer profiles with  $\delta_{99}$  of  $2h$  (Case A at  $Re_h = 3900$ , Case C at  $Re_h = 20K$ ), i.e. the cube is immersed in the boundary layer, and  $\delta_{99}$  of  $0.25h$  (Case B at  $Re_h = 3900$ , Case D at  $Re_h = 20K$ ), i.e. the cube extends through the boundary layer. These boundary layer thickness are selected because they represent the limiting cases of an obstacle

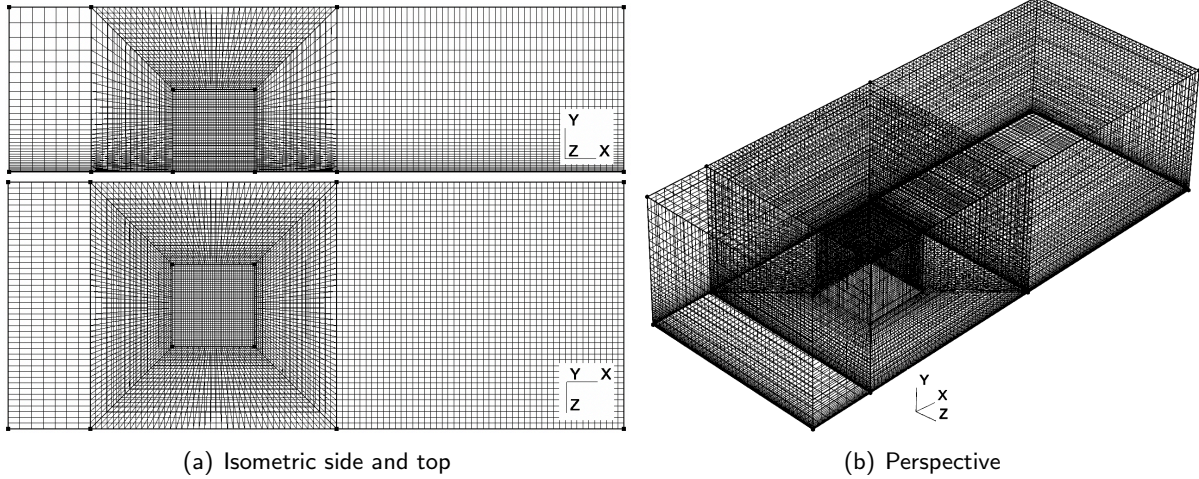


Figure 1: Surface mesh topology for wall-mounted cube DNS as constructed in Gmsh [65]. Outer mesh dimensions are  $N_x = 91$ ,  $N_y = 33$ ,  $N_z = 44$ . Mesh focusing in the cube region use  $N_{cube} = 33$ , a cube wall-normal growth factor of 1.05, and a cube to boundary element number of  $N = 24$ .

experiencing a highly sheared and nearly uniform inflow. The Reynolds number based on the cube height and maximum inflow velocity is  $Re_h = 3900$ . Note that a single  $Re_h$  is bit misleading due to the large disparity in inflow conditions. For instance, the  $Re_h$  for case A based on the local  $y$ -dependent inflow velocity at the cube height would only  $\approx 2900$ . Based on the bulk velocity, case A  $Re_h \approx 2500$  while case B  $Re_h = 3700$ . Despite the small domain and simple boundary conditions, the bulk features of interest for bluff-body type flows are captured in this model problem.

The spectral element code Nek5000 [66] is selected for its excellent scalability. For the DNS, approximately 240K 9th order spectral elements are used to discretize the domain with the mesh topology shown in Fig. 1. The grid has been carefully constructed with a target of keeping the Kolmogorov length scale ( $\eta = (\nu^3/\varepsilon)^{1/4}$ ,  $\varepsilon = 2\nu\langle\partial_j u'_i \partial_j u'_i\rangle$ ) to grid ratios in all directions above  $3/(2\pi) \approx 0.48$  to ensure all dissipative scales of motion are resolved [63]. For evaluations with the spectral element code used here, we have assumed the smallest resolvable length scale as  $\Delta = L_e/p$ , where  $L_e$  is the element size in each direction and  $p$  is the element polynomial order. The vertical direction ( $y$ ) was found to be the least resolved orientation with a minimum  $\eta/\Delta_y$  ratio of 0.49 which safely exceeds the optimal level for resolution of all viscous scales of motion. This minimum ratio occurs offset from the cube surface in the wake. However, for the  $\delta_{99} = 0.25h$  case, the ratio drops to 0.35 at the same vicinity. Thus, there is a small region in that case which may be considered marginally a DNS. However, with the majority of dissipation occurring in scales of motion great than  $15\eta$  [67], the effects can be assumed to negligible. The wall-normal location of first element quadrature point is at a maximum of just over unity at the forward corners of the cube but is generally 0.1 – 0.3 along the cube surface and wake. While a  $\Delta^+ > 1$  is usually not acceptable for a DNS, the region of such values are highly localized to edges. Edges and corners for finite element methods are singular location and therefore we cannot actually expect to apply standard mesh quality metrics to such locations.

For the WRLES, approximately 300K 7th order spectral elements are used to discretize the domain with the same basic mesh topology shown in Fig. 1 but a larger domain. The grid was constructed based on scaling up from a WRLES simulation which accurately reproduced the DNS results for the small domain at  $Re_h = 3900$  (results shown in §4) with some  $70\times$  total reduction in mesh size. Using the wall-adapting local eddy (WALE) model [68], grid requirements in each direction were scaled-up

using basic  $\Delta \sim Re^{3/4}$  [34]. Final grid dimensions are as follows: outer mesh  $N_x = 189$ ,  $N_y = 26$ ,  $N_z = 29$ , mesh focusing in the cube region use  $N_{cube} = 29$ , a cube wall-normal growth factor of 1.2, and a cube to boundary element number of  $N = 74$ . In general, element growth factors should be kept below 1.1 however, this rule-of-thumb is due to dispersion errors present with lower-order numerics. The higher-order spectral numerics of NEK5000 exhibits much less dispersion errors with the zero group velocity occurring at nearly  $\kappa \approx \pi/L_e$  instead of  $\kappa = 0.5\pi/L_e$  for second-order numerics where  $\kappa$  is the local wavenumber. Thus, more rapid element growth is acceptable. Again, the first wall-normal quadrature point is generally around  $y^+ \approx 0.3$  with the exception very near the sharp leading edge of the cube.

No additional filtering or numerical dissipation is used in the simulations. A single cube-based convective time takes approximately 16K core hours on the ALCF CETUS platform with CFL numbers kept below unity everywhere in the domain. Statistics are gathered for 100 convective times,  $t_c$ , after four flow-throughs. A mixed method is used with causal time averaging, *i.e.* explicit advancement of the ordinary differential equation  $d_t\langle\phi\rangle = \frac{1}{T_a}(\bar{\phi} - \langle\phi\rangle)$ , using an averaging timescale of  $T_a = 10t_c$ , being performed throughout the simulation followed by averaging over fields sampled every  $5t_c$ . Without a homogeneous direction, local averaging should be performed over a period of time exceeding 100 convective times for bluff body flows [24]. Thus, our statistics gathering window is marginal but was selected due to computational resource limitations.

While the inlet velocity profiles, symmetry top boundary condition, low  $Re_h$ , smooth walls, and overall small domain are clearly not identical to true obstacle flows in an atmospheric boundary layers or elsewhere, the simulation is still representative of the characteristics of interest and may be used to guide and progress to modeled turbulence methods which will be computationally feasible.

## 4 Results

Detailed results are presented for the DNS while WRLES results focus on comparison with the lower  $Re$  DNS and the far wake. With the exception of illustrative contour plots of the velocity field, cube wall shear stress, and vortex identification, DNS is presented as line plots over specific directions and offsets along planes. Such presentation should aid in use of the data for quantitative comparison. Planes considered will be along  $z = (0.0, \pm 0.25, \pm 0.5, \pm 0.75$  and  $y = (0.25, 0.5, 0.75, 1.0)$ . Mean quantities presented include streamwise velocity, turbulent kinetic energy ( $k$ ), turbulent time and length scales, specific Reynolds stress components, turbulent production ( $\mathcal{P}_k$ ) and dissipation ( $\varepsilon$ ). Cube-surface shear stress contours are also provided. Finally, we examine the efficacy of standard eddy viscosity models when using exact  $k$ ,  $\varepsilon$ , and strain.

### 4.1 Bulk flow characteristics

We begin with the general flow structure differences between the two cases. References made other works are summarized in Table 1 as organized by ascending  $Re_h$ . The effects of the inlet profile are evidently significant on all the bulk flow features. The most striking difference is the shape of the cube-wake separation region (Fig. 2). While case B exhibit the classic separation bubble reported by many others, *e.g.* [21], case A results in a smaller, and almost cube-like (elevation-wise), separation region. Across the span, the smaller wake is triangular as opposed to the common ellipsoid shown by case B. Naturally, this result is consistent with the reduced total inflow momentum for the 2h case and the smaller amount of momentum flowing around the cube sides. Wake reattachment occurs downstream from the cube at  $1.1h$  for case A and  $1.9h$  for case B. Reattachment results for case B are close to values reported at  $Re_h = 29K$  and  $19K$  by Hearst *et.al.* [38] with both turbulent and laminar inflow conditions. Thus,

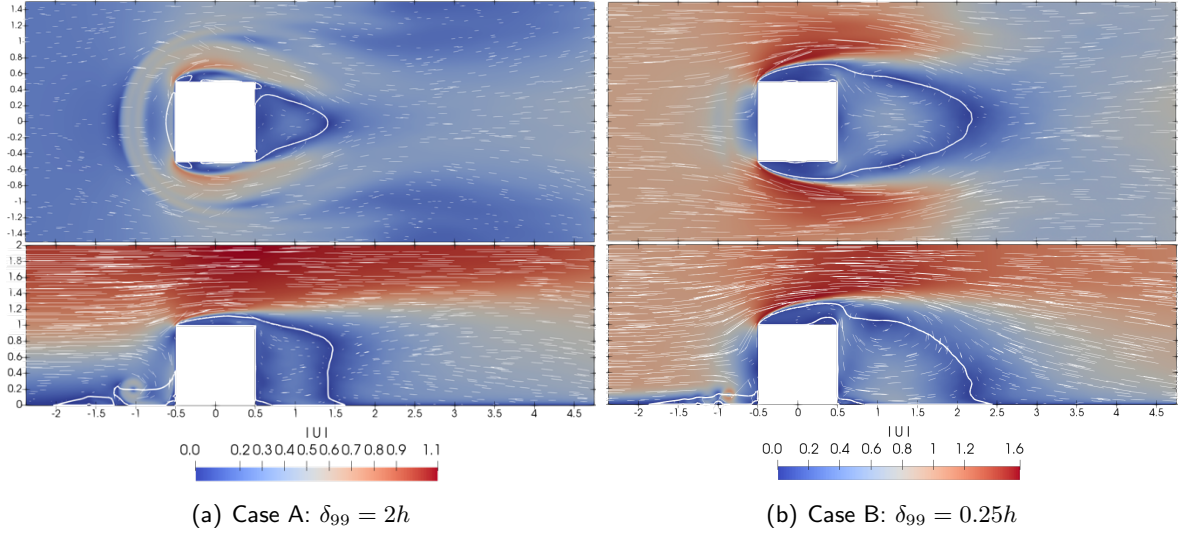


Figure 2: Time-average velocity magnitudes of DNS at  $Re_h = 3900$  at a elevation plane of  $y = 0.25$  (top) and a spanwise plane of  $z = 0$  (bottom) for both Blassius inlet conditions. Overlaid solid white line ( $u = 0$ ) highlights recirculation region shape at  $u = 0$ . Velocity field shown with white dashes. Wake reattachment occurs at  $1.1h$  (case A) and  $1.9h$  (case B) downstream from the cube.

we also see bulk flow features are apparently  $Re$ -insensitive with laminar inflow condition at  $Re_h \approx 4K$  consistent with the findings of [37] for turbulent inflow conditions. The difference between the fully-developed channel case of Martinuzzi *et.al.* [21] can be explained by the difference in domain boundary conditions. The slip condition used here more closely mimics a flat plate condition as opposed to a fully-developed channel. Case A resulted in the shortest reported reattachment length though most closely resembles that of the laminar inflow case of Daniels *et.al.* [58]. As the latter case falls in-between the two inflow cases examined here, their reported reattachment length being is consistent with the range we have measured. Not surprisingly, mean shear is the driving factor for wake behavior. Therefore, such results appear to be relatively insensitive to free stream turbulence, consistent with [38]. The swirling wakening velocity motion seen for case B in both views about  $x = 1.2$  is consistent with the large arc wake vortex reported by [21] and elsewhere. This structure is apparently much weaker for case A. Due to the small domain resulting in block-effects, cube-top speed-ups are quite significant with case B seeing a maximum mean streamwise velocity of 1.6.

Consistent with multiple sources in the literature, Reynolds number seems to have very little effect on the bulk flow characteristics (Fig. 3). Wake shape of the separation region and wake are nearly identical to the low  $Re$  cases. By changing the  $Re_h$  while maintaining identical inflow and zero mean freestream turbulence, the consistency across the range of  $Re$  considered here show that mean shear is the driving factor in wake behavior. However, we must stress that due to the different simulated domains, a strong comparison and definitive conclusion cannot be made. For instance, while the flow over the cube for case B accelerates to almost 1.6, it only achieves about 1.3 for case D. This is entirely due to increased blockage for the DNS with a smaller cross-sectional domain. Thus, we can expect some small differences in the recirculation shape due to different blockage ratios. We will return to the far wake behavior in §4.4.

The leading stagnation point shifts down from  $0.9h$  for case A to  $0.48h$  for case B as indicated by region of zero wall shear (Fig. 4 “front” panel). Also shown in Fig. 4 are secondary lower front face

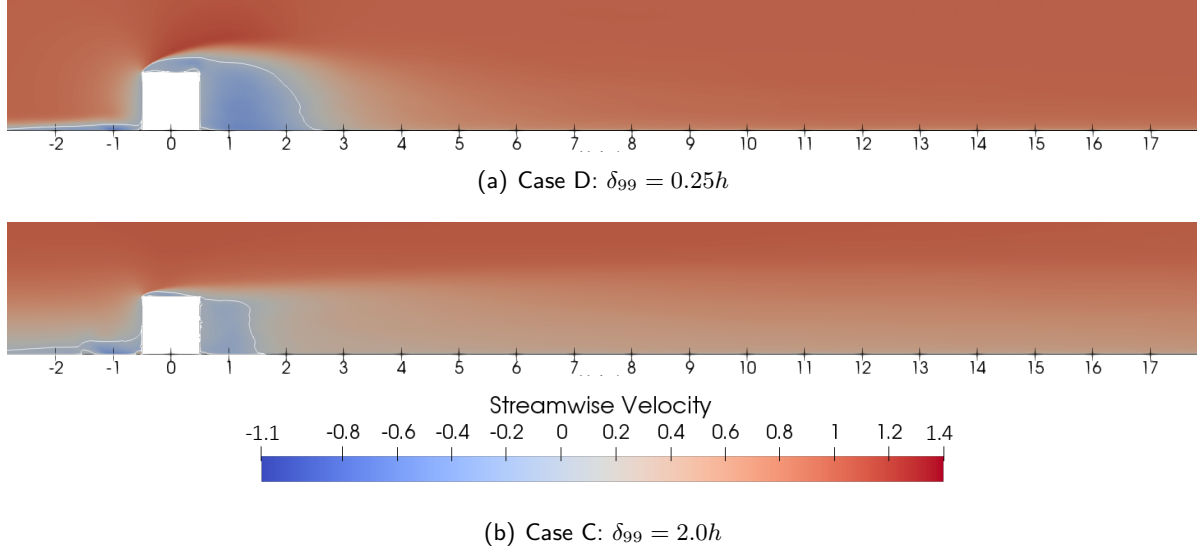


Figure 3: Time-average velocity magnitudes at a spanwise plane of  $z = 0$  for both Blasius inlet conditions at  $Re_h = 20K$ . Overlaid solid white line ( $u = 0$ ) highlights recirculation region shape at  $u = 0$ . Wake reattachment occurs at  $1.1h$  (case C) and  $1.9h$  (case D) downstream from the cube.

stagnation points. In response to the shifted stagnation point, the cube-top recirculation region for case B is larger than case A with a leading edge separated shear layer angle of about 30 degrees as opposed to 15 (side views of Fig. 2). These values, as well as the back face stagnation point, are nearly identical for  $Re_h = 20K$  (Fig. 6). Cube-top reattachment is apparent along the line of  $\tau_{wall} \approx 0$  for case B (Fig. 4 “top” panel). The profile of this reattachment is consistent with oil-film measurements at both  $Re_h = 40K$  and  $160K$  of [44] performed with a  $5h$  turbulent channel. Case A sees reattachment only at the trailing edge and experiences a band of strong back-flow just before the trailing edge. Reattachment is present for both  $Re_h = 20K$  cases but not over the entire span of the cube top. The significantly more energetic recirculation region of case B indicated by Fig. 2 is made evident by the back-face shear stress contours (Fig. 4 “back” panel) with case B seeing over an order-of-magnitude increase in peak wall shear. However, rear face reattachments are nearly identical at  $x \approx 0.16$  and agree with all reported except [21]. Contrary to the rear-face, the side faces for case A actually see elevated wall shear stress with a complex two-lobe pattern (Fig. 4 “sides” panels). We will return to the side-faces later in this paper and only point out that the two  $Re$  cases see similar patterns though the peak shear stress is shifted forward for case C in comparison with case A. The overall complexity in wall shear stress displayed in Fig. 4 and 6 highlights the difficulty of using wall models for LES for bluff-body flows. Naturally, the higher  $Re$  cases see higher peak shear stresses of approximately  $5\times$  the lower cases.

The first forward separation point appears to be relatively insensitive to the inflow profile with both low  $Re$  cases occurring at about  $x \approx 1.45$ . However, there are multiple forward separation/saddle points, and this may explain why the observed values agree well with some sources [22] but do not agree well with others [21,23], *i.e.* the true first separation is very weak and hard to detect. The higher  $Re$  cases see nearly double forward separation length though this is more likely due to the larger domain used in these cases and not actual  $Re$  effects. The classic primary horse vortex is visible in mean velocity profiles (Fig. 2) and is stronger, smaller and closer to the cube for the case B. The full, and rather complex, horseshoe vortex system is evident when plotting iso-surfaces of Q-criterion (Fig. 5). The main vortex is shown by the highest vortex magnitude of the iso-surface. There appear to be three classic horseshoe vortices for case A while case B sees some six vortices. Interestingly, case A exhibits a second strong

<i>Source</i>	$Re_h(K)$	Inflow	$x_r$	$x_s$	$y_{sf}$	$y_{sr}$
Yakot <i>et.al.</i> [23]	1.9	FDC ( $H = 3h$ )	1.5	1.2	0.65	0.15
Case A	2.9	Laminar ( $\delta_{99} = 2h$ )	1.1	1.5	0.9	0.15
Daniels <i>et.al.</i> [58]	3.0	Laminar ( $\delta_{99} = 1h$ )	1.43	2.1	0.81	0.18
Daniels <i>et.al.</i> [58]	3.0	Flat plate ( $\delta_{99} = 0.42h$ )	1.45	1.4	0.67	X
Case B	3.9	Laminar ( $\delta_{99} = 0.25h$ )	1.9	1.4	0.48	0.18
Meinders <i>et.al.</i> [22]	7.0	FDC ( $H = 3.3h$ )	1.5	1.4	X	X
Hearst <i>et.al.</i> [38]	11	Flat plate ( $\delta_{99} = 0.5h$ )	1.9	X	0.66	X
Case C	15	Laminar ( $\delta_{99} = 2h$ )	1.1	3.2	0.89	0.1
Case D	20	Laminar ( $\delta_{99} = 0.25h$ )	1.9	2.9	0.5	0.15
Lim <i>et.al.</i> [25]	20	ABL ( $\delta_{99} = 3h$ )	1.56	X	0.73	X
Hearst <i>et.al.</i> [38]	29	Flat plate ( $\delta_{99} = 0.5h$ )	1.88	X	0.65	X
Martinuzzi <i>et.al.</i> [21]	40	FDC ( $H = 2h$ )	1.61	1.02	0.5	0.1

Table 1: Bulk flow characteristics for simulations presented here in the context of existing works as organized by ascending  $Re_h$ . For the purpose of classification, we have use  $Re_h$  based on the cube-height velocity for the cases performed here. Column labels: wake reattachment length ( $x_r$ ), first upstream separation point ( $x_s$ ), front face stagnation point ( $y_{sf}$ ), and rear cube stagnation point ( $y_{sr}$ ). Fully developed channel (FDC) inflow characterized by  $Re_h$  and channel height,  $H$ . A wind tunnel simulated neutral atmospheric boundary layer is indicate by ABL. Lengths reported from cube surface or ground.

vortex very near to the cube that is not apparent in Fig. 2 which wraps around to the wake. Further, a second inner vortex structure tightly follows the cube surface for case A and is incapsulated by the first inner vortex. Such near-cube vortex structures are not visible for case B. The higher  $Re$  cases exhibit similar near-cube vortex structure but only show the main large horseshoe vortex. The aforementioned cube-surface innner vortex structure for case A is present for case C but seems to terminate closer to the front of the cube. This shift explains the shift in wall shear stress along the cube sides seen in figures 4 and 6. The smaller number of horse vortices and general reduced coherence for the high  $Re$  cases is due to a combination of the higher momentum and longer inflow length upstream of the cube which allows turbulence to form near the wall which is not evident for the low  $Re$  cases.

## 4.2 Mean streamwise velocity

Figure 8 shows mean wake streamwise velocity profiles offset by distance from the cube center for elevations of 0.1, 0.25, 0.5, 0.75, 1.0, and 1.25 $h$ . Both cases are displayed (A in green on the bottom and B in blue on the top) and reflected about the centerline to show the relative symmetry in the mean velocity and contrast the different wake structures. For both cases, a complicated streamwise flow pattern is present close to the wall with kinks and sharp transitions at locations of  $x = -0.5$  to 1.0 and  $y = 0.1$  that are indeed part of the mean and are statistically well converged with no double lines from plotting of both sides visible. An apparent high speed band forms around 0.2 $h$  away from the cube surface and wraps in towards the center in the wake. Smaller low-speed bands flank this accelerated region. However, by  $y = 0.25h$  for case B and  $y = 0.5h$  for case A, this more complex flow structure has been smoothed out. Clearly, this behavior is due to the horseshoe vortex systems. From Fig. 2b, we see the main horseshoe vortex terminates before  $y = 0.25h$  for case B so that there is no similar complex streamwise flow pattern observed for case B in Fig. 8b. For both cases, at  $x = 0$  for multiple elevations, back flow is evident with the mean streamwise velocity being negative. However, this is only present for case A at  $y = 0.5$  and 0.75 while it remains a prominent feature for all case B elevations.

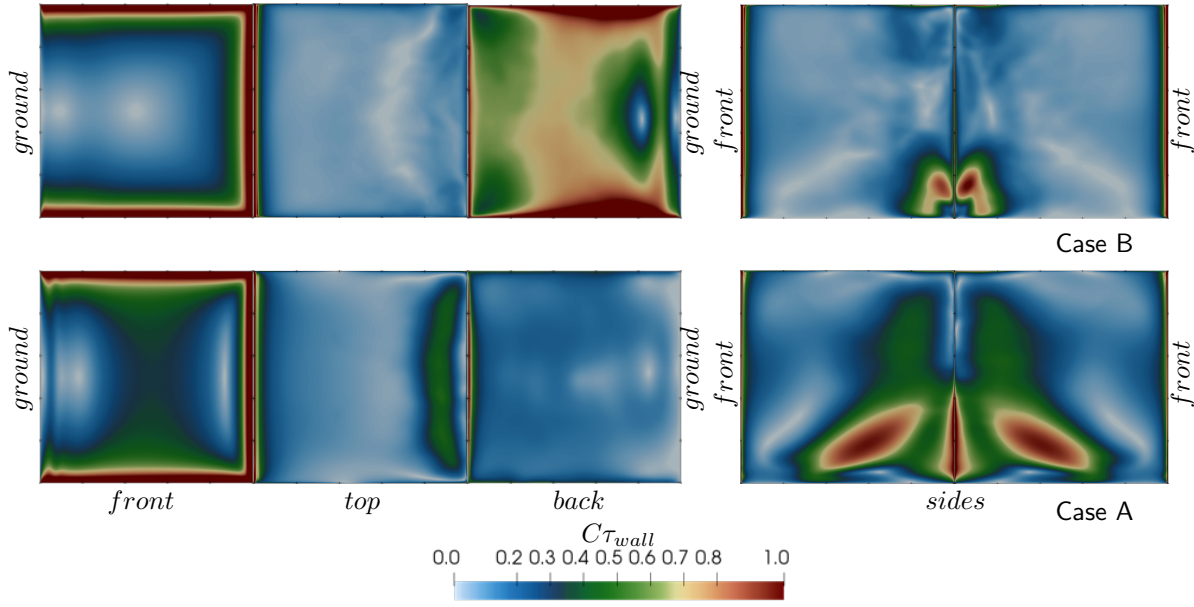


Figure 4: Wall shear stress magnitude at cube surfaces for  $Re_h = 3900$ . Multiplicative constant for case A/front  $C = 50$ , case B/front  $C = 20$ , and for all others  $C = 100$ . Cube face labels correspond to planes as “front”  $x = -0.5$ , “top”  $y = 1.0$ , “back”  $x = 0.5$ , and “sides”  $z = \pm 0.5$ . Lines of  $y = 0$  are indicated by the “ground” label. Regions of stagnation and reattachment where  $\tau_{wall} \approx 0$ .

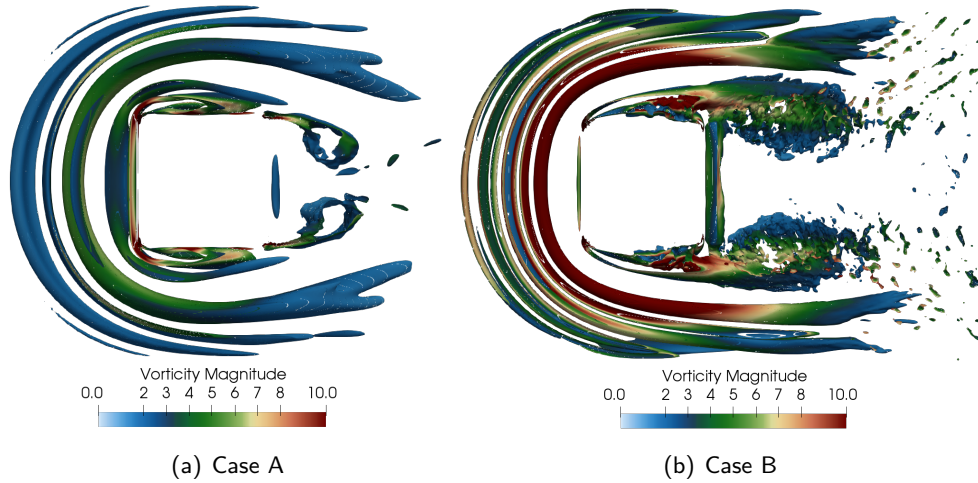


Figure 5: Horseshoe vortex system at  $Re_h = 3900$  shown by Q-criterion iso-surface (0.5) colored with vorticity magnitude. Displayed from bottom looking up over a thin slab of  $\Delta y = 0.25$ . Main horseshoe vortex for each case indicated by highest vorticity magnitude upstream of the cube.

Further, while back flow is present all the way to the end of the cube ( $x = 0.5$ ) for case B, the flow has reattached over the cube sides by its trailing edge for all elevations for case A. The wake width for case B grows over the cube trailing edge to  $0.5h$  downstream to a fairly constant size of at about twice the cube width for all streamwise locations aft of the cube. For case A, the wake width decreases over the same stretch to about the cube width. Finally, both the relative recirculation back flow velocity and side acceleration are significantly higher for case B.

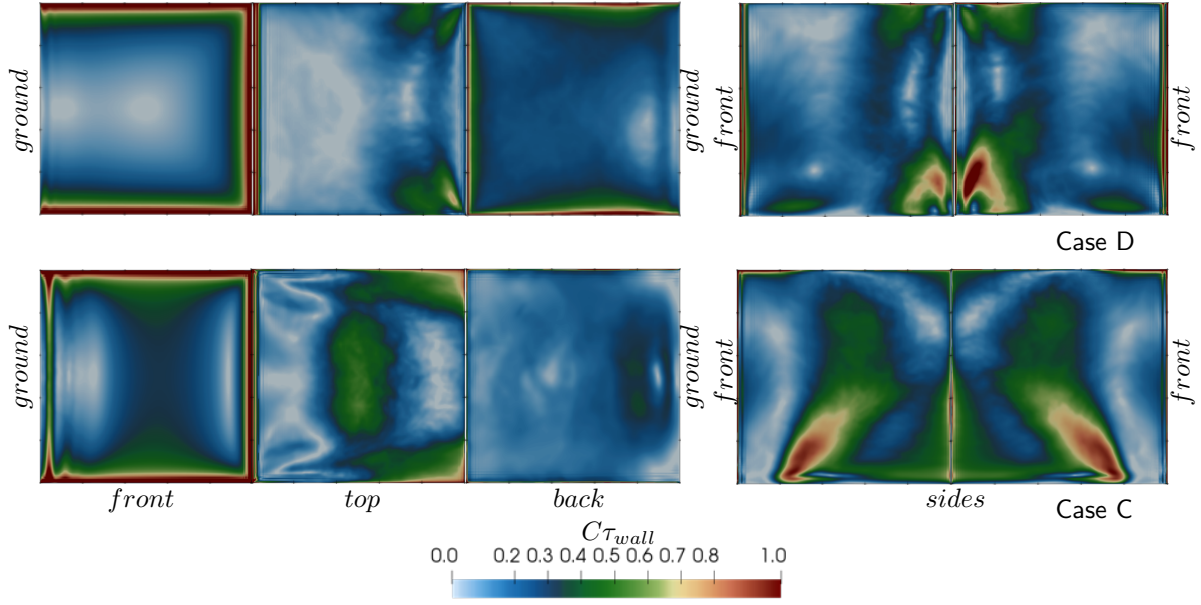


Figure 6: Wall shear stress magnitude at cube surfaces for  $Re_h = 20K$ . Multiplicative constant for case C/front  $C = 20$ , case D/front  $C = 10$ , C/top  $C = 50$ , D/top  $C = 50$ , C/back  $C = 100$ , D/back  $C = 25$ , C/side  $C = 35$ , and D/side  $C = 50$ . Cube face labels correspond to planes as “front”  $x = -0.5$ , “top”  $y = 1.0$ , “back”  $x = 0.5$ , and “sides”  $z = \pm 0.5$ . Lines of  $y = 0$  are indicated by the “ground” label. Regions of stagnation and reattachment where  $\tau_{wall} \approx 0$ .

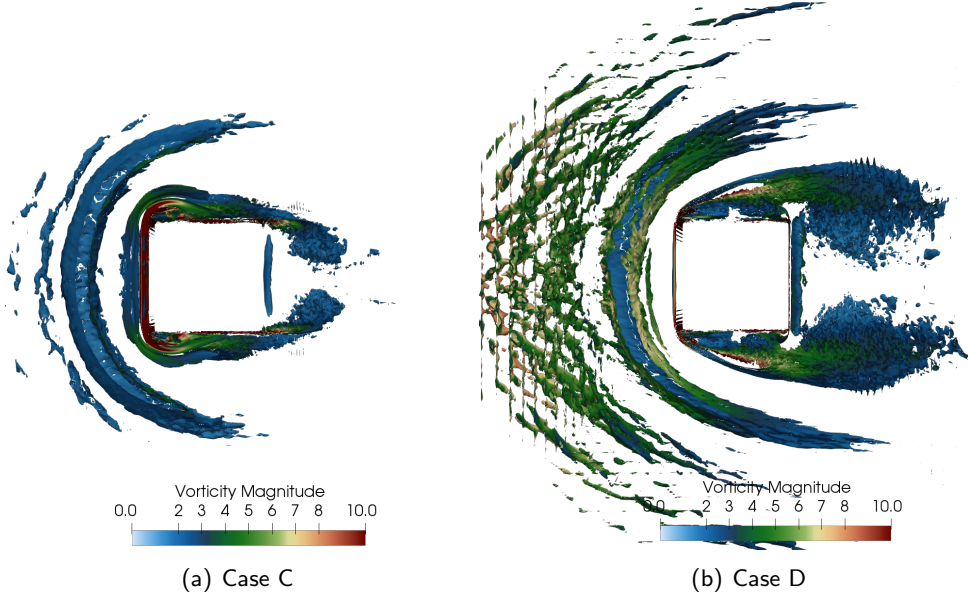


Figure 7: Horseshoe vortex system at  $Re_h = 20K$  shown by Q-criterion iso-surface (0.5) colored with vorticity magnitude. Displayed from bottom looking up over a thin slab of  $\Delta y = 0.25$ . Main horseshoe vortex for each case indicated by highest vorticity magnitude upstream of the cube.

Figure 9 shows mean wake streamwise velocity profiles offset by distance from the cube center for spanwise planes of  $z = 0.0, \pm 0.25, \pm 0.5$ , and  $\pm 0.75h$ . Symmetry planes are averaged here for plot line

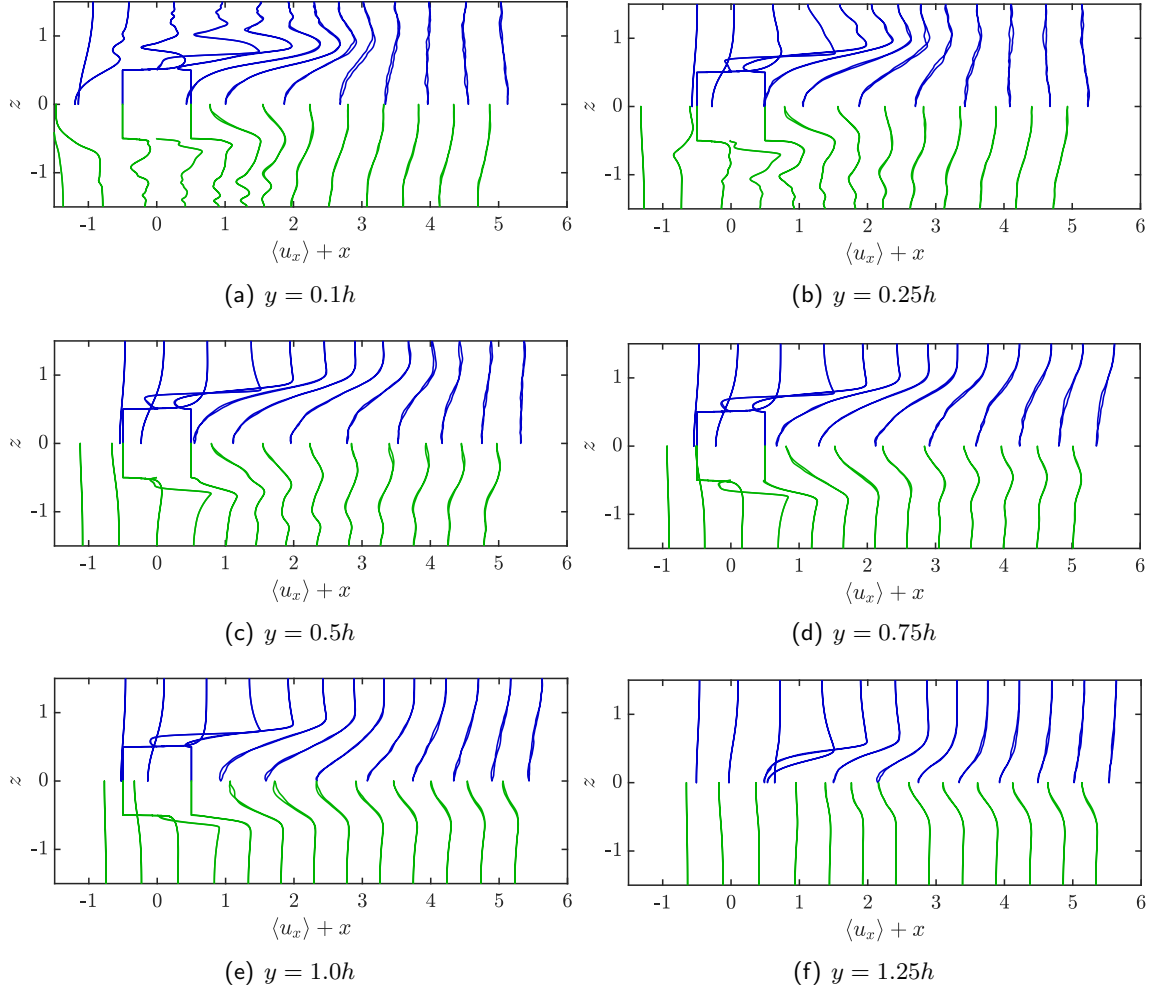


Figure 8: Time-average streamwise velocity profiles for case A (—) and case B (—) at streamwise increments along elevation planes offset by  $0.25h$  (exception of first plane at  $y = 0.1$ ). Streamwise profiles shown correspond to  $x = -1.5$  to  $4.5$  in  $0.5h$  increments. Both sides of the velocity profiles are plotted to show symmetry of the mean wake.

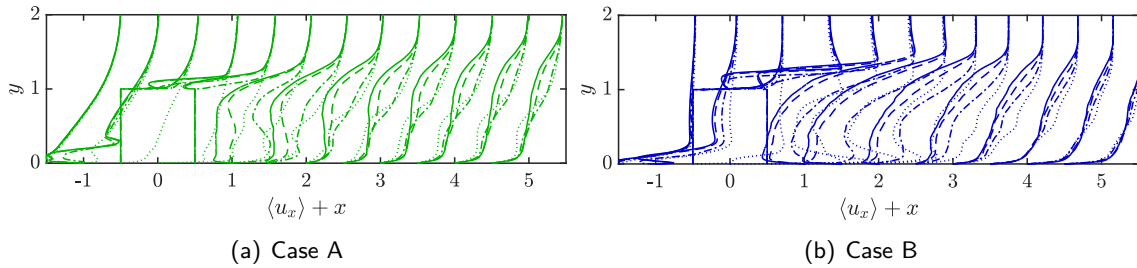


Figure 9: Time-average streamwise velocity profiles for case A (—) and case B (—) at streamwise increments of  $0.5h$  along spanwise planes of  $0.0h$  (—),  $0.25h$  (---),  $0.5h$  (-·-), and  $0.75h$  (···) offset from the center of the cube.

type clarity. The first streamwise location is a slightly perturbed inlet profile for each case. The side

profiles at  $z = \pm 0.75$  retain the near-inlet profile up to  $x = 0.5$  for case A but only up to  $x = -0.5$  for case B. For both cases, a region of back flow near the wall is present at  $x = -1.0$  due to the main horseshoe vortex. Consistent with Fig. 2, this region is smaller and more intense for case B. Contrary to along the sides as observed in Fig. 8, case A does exhibit back flow all the way the cube trailing edge at the cube top consistent with wall shear stress (Fig. 4). Though the flow has reattached on the cube top for case B as previously discussed, there is apparently still significant back-flow above the reattachment as shown by the  $x = 0.5$  and  $z = 0.0, \pm 0.25, \pm 0.5$  profiles. The wake of case A is characterized by uniform velocity profiles at  $z = 0.0$  and  $0.25$  below the cube height in the recirculation region with gradual deviation further downstream. Case B shows an elevation-dependent recirculation region with the highest backflow velocity at approximately  $y = 0.2$  along the spanwise center. The high speed bands along the cube edge described above for case A are highlighted at  $x = 0.5$  and  $z = 0.5$  with a peak at about  $y = 0.2$ . High speed bands are also present in case B but are confined to the near wall region of  $y < 0.2$  and are further away from the cube and visible in the  $z = 0.75$  profiles. There is a drastic transition from the nearly undisturbed inlet profile at  $x = -0.5$  to  $x = 0.0$  at  $z = 0.75$  near the wall with a large degree of acceleration evident for case B. For both cases, the streamwise velocity is nearly uniform across the span of the domain by  $x = 4.5$ .

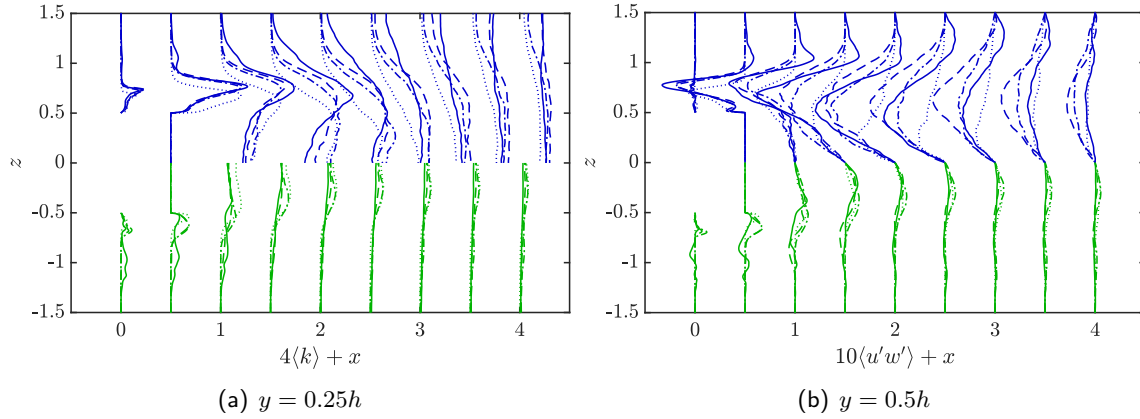


Figure 10: Time-average turbulent kinetic energy and  $\langle u'w' \rangle$  Reynolds stress profiles for case A (—) and case B (---) at streamwise increments of  $0.5h$  along elevation planes of  $0.25h$  (—),  $0.5h$  (---),  $0.75h$  (— · —), and  $1.0h$  (····). Note different multiplication factors for each case.

### 4.3 Mean turbulence

Figure 10a shows mean wake turbulent kinetic energy profiles, amplified by a factor of four for emphasis, offset by streamwise distance from the cube as a function of elevation across the span of the domain. Naturally, the higher overall momentum flow of case B yields significantly more turbulence at all elevations and streamwise locations. Case B peak turbulence is approximately six times that of case A. Peak turbulence for both cases occurs at the cube trailing edge centered about the separation shear layer with small drops near the top of the cube. Peak case A turbulence is very near the cube surface and offset by less than  $0.1h$  while being further away and offset by over  $0.25h$  for case B. Turbulence is concentrated along the recirculation region edge and becomes uniform across the wake further downstream. There appears to be turbulence produced near the wall and far from the cube wall for case A. As the separated shear layer does not extend this far, such “turbulence” is likely be due to unsteady vortex motion being included as turbulent fluctuations with the time averaging used here. We will return to this point later. For both cases, the turbulence is nearly uniform across the domain by streamwise location of  $x = 4$ .

However, the slight peak at about  $x = 0.25$  and  $y = 0.5$  seems to persist for case A.

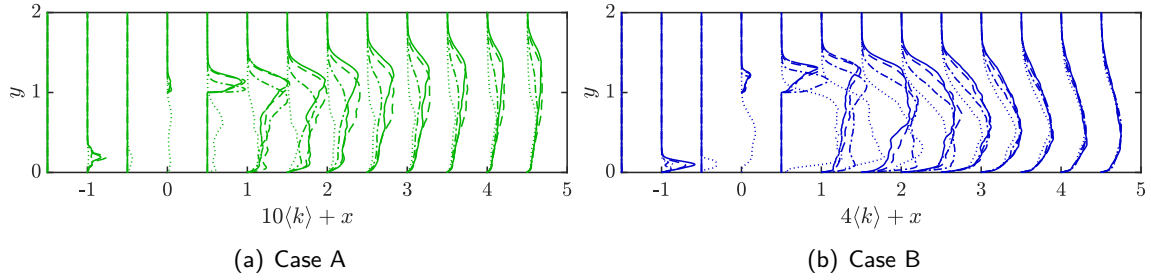


Figure 11: Time-average turbulent kinetic energy profiles for case A (—) and case B (—) at streamwise increments of  $0.5h$  along spanwise planes of  $0.0h$  (—),  $0.25h$  (—),  $0.5h$  (—), and  $0.75h$  (···) offset from the center of the cube. Note different multiplication factors for each case.

Turbulent kinetic energy profiles are further shown in Fig. 11 as a function of elevation for spanwise planes of  $z = 0.0, \pm 0.25, \pm 0.5$ , and  $\pm 0.75h$ . Again, the peak turbulence occurs at the trailing edge of the cube top and is offset by the shear layer location. For case A, peak turbulence occurs at the edge of the cube ( $z = 0.5$ ) and then rapidly decreases by  $z = 0.75$ . However, for case B, we see the peak turbulence occurring along spanwise plans offset from cube. At  $z = 0.75$ , the cube-side turbulence is nearly uniform across the cube height until rapidly decaying at  $y = 0.1$ . Only minimal turbulence is observed across the same location for case A. This difference in turbulence concentration leads to the different wake profiles of  $k$  spreading from above the cube height in case A with very little produced below the cube height while being strongly concentrated below the cube height in case B. Naturally, these differences are due to significantly decreased momentum flowing around the cube sides in case A. The upstream profiles at  $x = -1$  are interesting as both cases show turbulence focused near the wall in the horseshoe vortices. This is again likely due to unsteadiness in the vortices and not actual turbulent production. For both cases, turbulence does not reach the upper boundary in the simulated domain though case A reaches approximately  $y = 1.8$  while case B turbulence stays closer to the ground. Such wall normal spreading is certainly retarded by the symmetry boundary condition and the resulting freestream velocity which is higher than would be without the small domain and symmetry boundary condition.

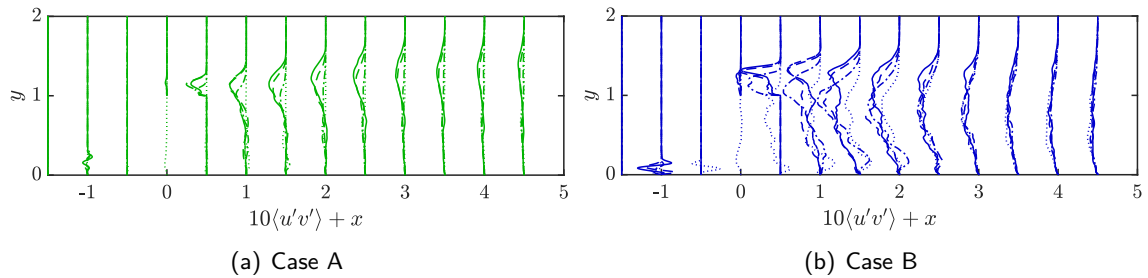


Figure 12: Time-average  $\langle u'v' \rangle$  Reynolds stress profiles for case A (—) and case B (—) at streamwise increments of  $0.5h$  along spanwise planes of  $0.0h$  (—),  $0.25h$  (—),  $0.5h$  (—), and  $0.75h$  (···) offset from the center of the cube.

Of course, turbulent kinetic energy by itself does not govern turbulent transport. The spanwise gradient of the  $\langle u'w' \rangle$  shear stress will be the primary contributor to the turbulent flux in the streamwise momentum

direction along the sides of the cube/wake while the elevation gradient of the  $\langle u'v' \rangle$  shear stress will contribute to the turbulent flux in the streamwise momentum direction along the top of the cube/wake. Through these stress components, high speed freestream momentum is transported into the wake region. Specific shear stress components profiles are presented in Fig. 10b ( $\langle u'w' \rangle$ ) and Fig. 12 ( $\langle u'v' \rangle$ ). Profiles are selected so that they align with the gradient directions of interest for streamwise momentum turbulent flux term. Positive gradients of  $\langle u'w' \rangle$  along the profiles indicate an acceleration in the streamwise velocity due to turbulent mixing. From Fig. 12 we again see peak shear stress occurring at the trailing edge of the cube. Within this peak, *i.e.* in the separation and recirculation region, increasing  $\partial_z \langle u'w' \rangle$  shows a transfer of momentum into the cube wake. Outside of this peak, increasing  $\partial_z \langle u'w' \rangle$  translates to large bands of deceleration as the higher momentum fluid is mixed with lower momentum wake. Moving downstream of the cube, the behavior decreases in magnitude but broadens across the span. The  $\langle u'w' \rangle$  stress component drops rapidly in magnitude for case B from  $x = 1.5$  to 2. From Fig. 2b we see this is due to the drop-off of the recirculation region.

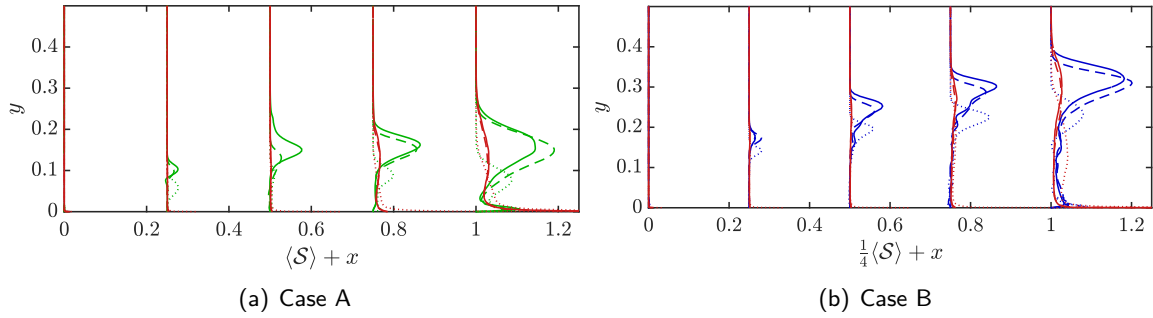


Figure 13: Time-average turbulent kinetic energy source terms, production  $\mathcal{P}_k$  (---) and ( $-$ ), and dissipation  $\epsilon$  (—), profiles for case A and case B normal to the cube *top* at streamwise increments of  $0.25h$  offset from the cube edge. Spanwise planes of  $0.0h$  (—),  $0.25h$  (---), and  $0.5h$  (· · ·) offset from the center of the cube. Note different multiplication factors for each case.

Figure 12 shows  $\langle u'v' \rangle$  across ground-normal profiles. While the magnitude of peak  $\langle u'w' \rangle$  are drastically different for case A and B ( $\sim 7\times$ ), the peak magnitudes of  $\langle u'v' \rangle$  are closer ( $\sim 2\times$ ). This difference in the relative shear stress magnitudes is due to the amount of momentum passing over the cube top being more similar for the two cases than what passes around the sides. Again, we see deceleration of the fluid above  $\langle u'v' \rangle$  peaks with acceleration in the separation and recirculation regions. However, the mixing for case A stays focused (though decreasing in magnitude) and moves toward the top of the domain while, for case B, becoming more diffuse and moving towards the ground. This behavior is due to the mean inflow gradients in case A with the majority of momentum above the cube whereas the momentum passing over the case B cube is nearly uniform over its height. The texture of the  $\langle u'v' \rangle$  are indicative that the statistics gathering window should be increased for higher-order statistics. At  $x = -1$  we see again what is likely an artifact of the unsteady horseshoe vortices. A vortex with shift back and forth in the streamwise direction with some unsteady period would register as a  $\langle u'v' \rangle$  due to the time averaging used here.

The last turbulence statistic we present are the source terms in the turbulent kinetic energy evolution, *i.e.* production and dissipation. Rather than displaying such quantities over the whole domain where they would be rather small, we restrict this analysis to cube-wall regions. Note that for this discussion, coordinate descriptions are shifted to the relative cube surface in question. Source terms along paths normal to the cube top are presented in Fig. 13 while paths normal to the cube sides are presented

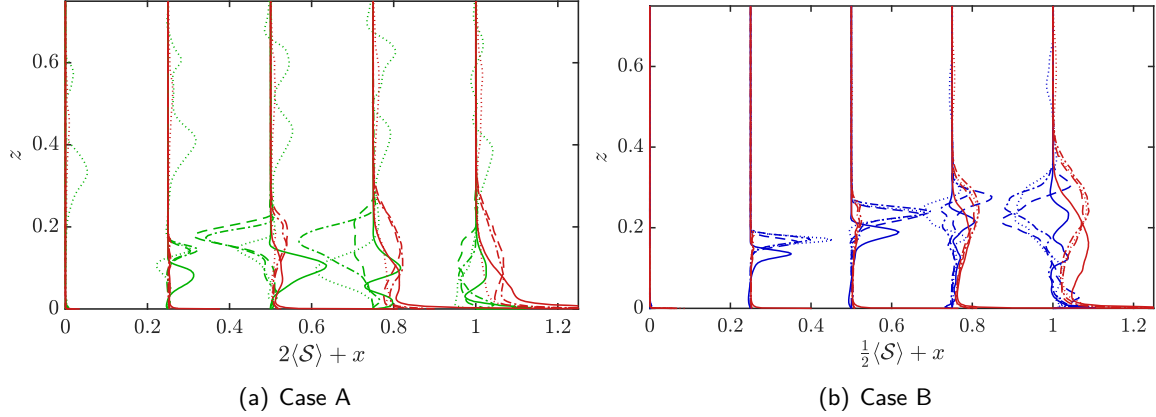


Figure 14: Time-average turbulent kinetic energy source terms, production  $\mathcal{P}_k$  (--- and (---)) and dissipation  $\varepsilon$  (—), profiles for case A and case B normal to the cube *side* at streamwise increments of  $0.25h$  offset from the cube edge. Elevation planes of  $1.0h$  (—),  $0.75h$  (---),  $0.5h$  (---), and  $0.25h$  (···). Note different multiplication factors for each case.

in Fig. 14. Not surprisingly, peak production is centered about the separation shear layer and follows a nearly Gaussian profile. For case A, the elevation of the peak becomes fixed at about  $z = 0.15$  by  $x = 0.5$ . The elevation of the peak continues to grow for case B. For both cases, the peak is not at the centerline but shifted towards  $z = \pm 0.25$ . Moving further from the cube center results in a sharp decline in production and the peak shifting towards the cube surface. Case B sees over  $4\times$  the peak production of case A. Shear layer dissipation at the interior of the surface is much smaller over the cube and begins to emerge as a shallow Gaussian following the peak production by the cube trailing edge. However, the dissipation does spike at the trailing edge. This is likely due to sharp edges being singular points where any oscillations in the numerical solution will be included as turbulent fluctuations and register as a dissipation due to time averaging. The cube edge dissipation does shift further towards the surface and does not simply follow the peak production like the other spanwise locations.

The side-normal source term profiles (Fig. 14) are significantly more complicated. For case B, at  $x = 0.25$  and  $0.5$ , the behavior is similar to the cube top behavior with Gaussian production-profiles moving away from the surface. For case A, this behavior is only observed at  $x = 0.25$  and  $0.5$  and at the cube height of  $y = 1$ . At all other stations, production oscillations are observed even with relatively strong negative production at  $x = 0.5$  and  $0.75$  for case A and at  $x = 1$  for case B. Case A also displays positive production regions offset a significant distance from the cube surface near the ground. Both these results would seem to be physically inconsistent with separate shear layers. Such negative production would represent transfer of energy from turbulent fluctuation to the mean. Such negative production was also reported in the similar study of Yakhot *et.al.* [23] however, with a fully-developed turbulent inflow, they observed the strongest negative production in front of the cube and only small amounts on the side. Recently, Cimarelli *et.al.* [69] have also observed such negative production in bluff-body flows near the leading edge of the structure. They argue this phenomena is due to positive correlation between the Reynolds stress and vertical mean shear. Spectral analysis of the Reynolds stress showed a large separation of scales between a low frequency peak, which was responsible for negative production, and high frequency turbulence, which resulted in a smaller positive production. This suggests negative production can result where long turbulent structures interact with regions with two- or three-dimensional mean gradients. Given that the horseshoe vortices wrapping around the cube sides identified for case A will induce secondary motion in the vertical direction along the cube surface, this mechanism

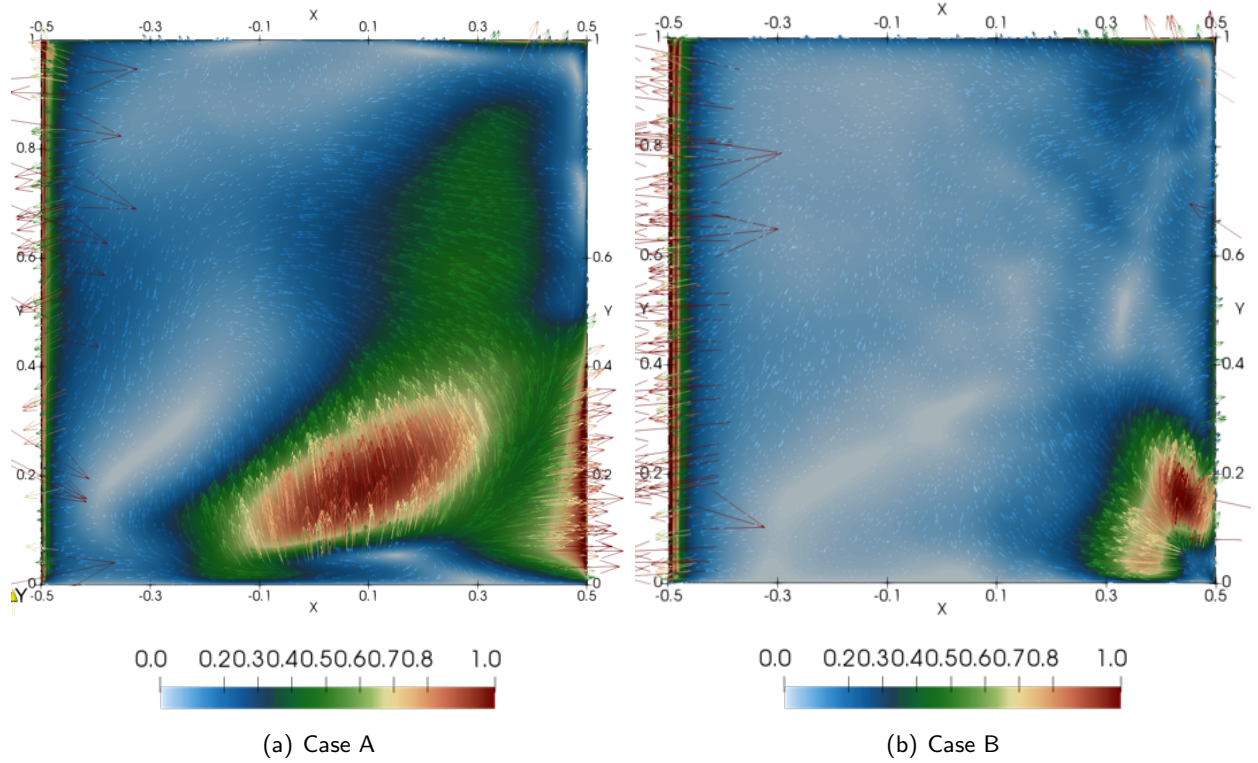


Figure 15: Wall shear stress magnitude (multiplied by a factor of 100) and wall normal gradient vector field at cube side. Regions of high shear (excluding leading edge) are primarily due vertical acceleration.

seem plausible. The lack of these structures for case B is then consistent with a much smaller level of negative production. Indeed, gradient vector fields along the cube sides reveals the high wall stress seen for case A is due to positive vertical shear at the surface (Fig. 15). This high shear is due to the inner-near cube vortex structure identified for case A in Fig. 5 and is not seen for case B.

The proposed negative production mechanism requires Reynolds stress to activate. For case B, the uniformly positive production across all elevations at  $x = 0.25$  and  $0.5$  would provide the necessary turbulence. However, while there is some positive production early with case A, especially towards the top of the cube, there does not seem to be enough to justify the large amounts negative production at  $x = 0.5$  or even the small amount very near the surface at  $x = 0.25$ . It may be that turbulence is being generated very near the wall and being convected upward. It is also possible we are observing a combination of an actual complex phenomenon and artifacts of unsteady flow structures being erroneously considered turbulence by time-averaging. The positive production regions offset from the surface of case A are almost certainly due to this statistical corruption.

#### 4.4 Far wake

Rather than present a set of nearly identical velocity profiles for cases C and D, we instead focus on the wake recovery. Wake velocity and turbulence intensity as a function of distance from the cube are presented at the half-cube height and cube height for all cases in Figures 16 and 17, respectively.

Again, both near- and far-wake behaviors are drastically altered in response to the different inflows. Very little difference is observed for the different  $Re_h$  and what small differences are present are likely due

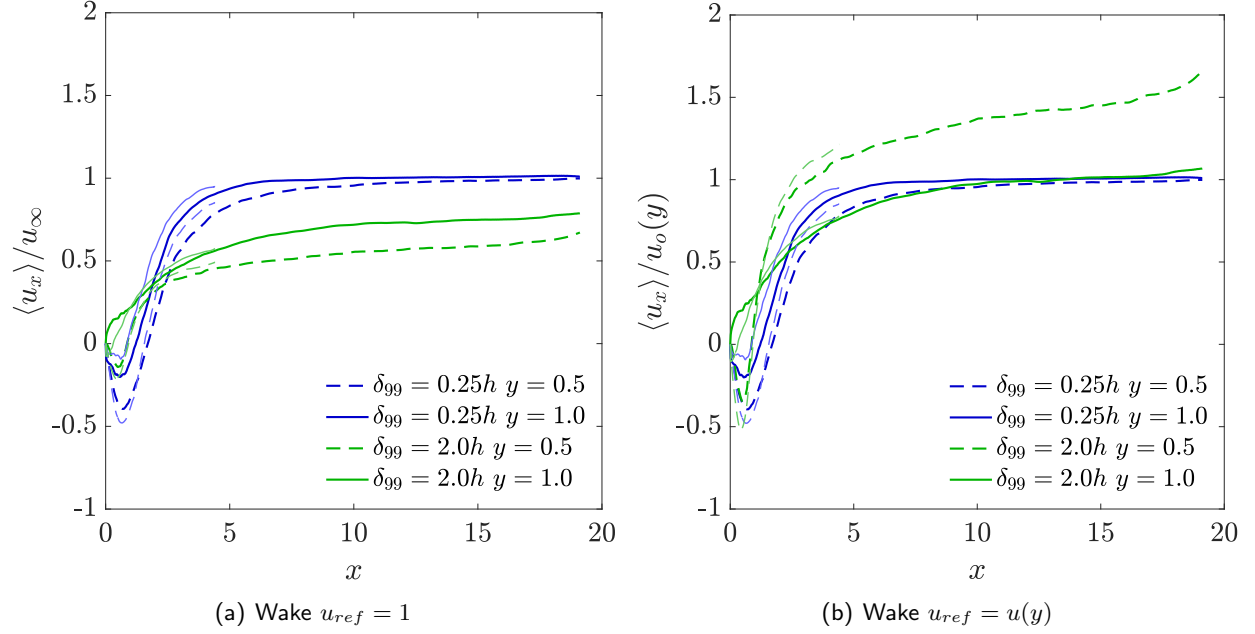


Figure 16: Mean wake velocity profiles along a centerline extending from the rear face of the cube at elevations of  $y = 0.5h$  and  $y = 1.0h$  for all cases (bold lines for  $Re_h = 20K$ ). The nearly uniform inflow case of  $\delta_{99} = 0.25h$  results in a rapid recovery of the wake by  $5h$  while the  $\delta_{99} = 2.0h$  sees a more gradual return but also exhibits a continual increase in momentum, especially at the  $0.5h$  elevation. The small difference in  $Re_h$  is likely due to blockage effects with the smaller DNS domain.

to the increased blockage of the DNS cases. The  $\delta_{99} = 0.25h$  cases exhibit stronger back flow in the separation bubble while the  $\delta_{99} = 2.0h$  cases only see a small amount at  $y = 0.5h$ . The wake for the  $\delta_{99} = 0.25h$  cases recovers rapidly to the full inlet value by  $5h$ . The  $\delta_{99} = 2h$  cases recovers at the cube height more slowly by  $10h$  but recovers more rapidly at the half-cube height achieving the inflow velocity by  $3h$ . After which, the flow continues to gradually accelerate at this height (Fig. 16b). The reason for this increase is apparent when examining the turbulence intensity along the same wake paths (Fig. 17).

The peak turbulence intensity is almost  $3\times$  higher for the  $\delta_{99} = 0.25h$  cases due to the additional momentum in the flows and resulting stronger shear and production around the cube. However, these high values are highly localized and rapidly decay to below the  $\delta_{99} = 2h$  values by  $10h$  downstream of the cube. Consistent with an axisymmetric jet [70], the turbulence intensity decays as  $x^{-1}$  for the  $\delta_{99} = 0.25h$  cases after the peak at about  $x = 1h$  downstream of the cube. The decay is more rapid than that of grid turbulence,  $\sim x^{-5/7}$  [71,72]. On the other hand, the  $\delta_{99} = 2.0h$  cases see a much more gradual decay of approximately  $x^{-0.2}$  and is more closely related to a mixing layer with no decay rate. Thus, we see the mean inflow shear is as, if not more, important than the three-dimensionality of the obstacle in determining the turbulence levels and decay rate in the wake. Though the peak turbulence and total momentum is lower for the  $\delta_{99} = 2h$  case, the mean shear imparted on the wake by the thicker inlet boundary condition results in sustaining of the wake turbulence. By the end of the domain for the WRLES, the  $\delta_{99} = 2h$  case has about  $5\times$  the turbulence. Thus, the continued increase in the streamwise velocity at  $y = 0.5h$  of the thick boundary layer case is due to sustained turbulent mixing of the high momentum fluid above the cube with the low momentum wake fluid. The shift in decay rate at about  $x = 5h$  for the case C is likely due to overall transition to a turbulent boundary layer.

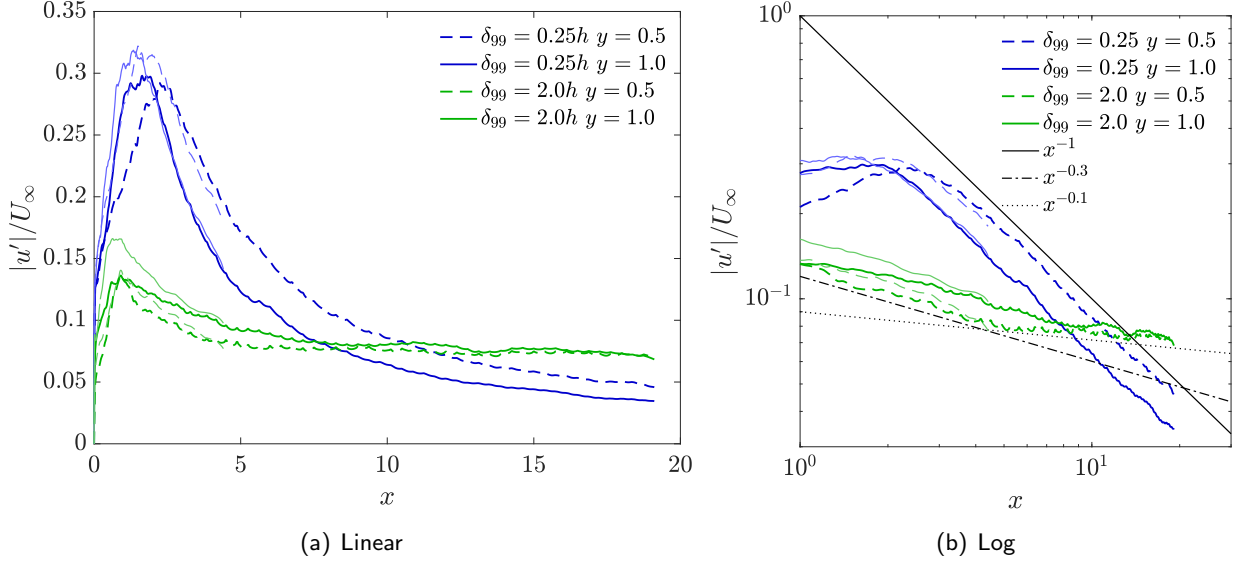


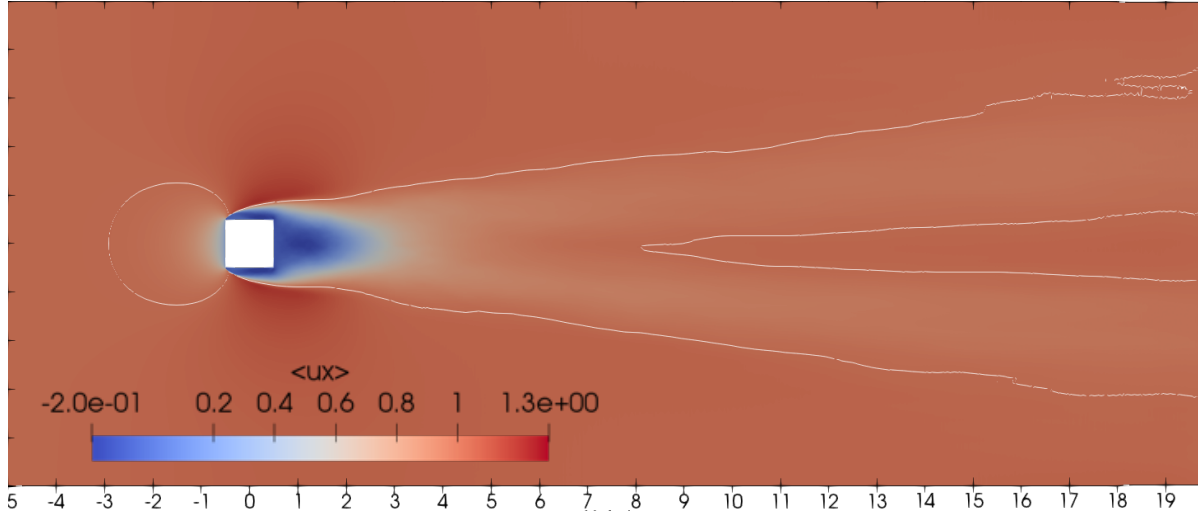
Figure 17: Wake recovery for mean turbulence intensity along centerline of simulated domains at elevations of  $y = 0.5$  and  $y = 1$  for all cases (bold lines for  $Re_h = 20K$ ). Though the  $\delta_{99} = 0.25h$  inlet sees a peak turbulence of  $5\times$  the  $\delta_{99} = 2.0h$  case, the mean shear present in the latter case sustains the wake turbulence throughout the domain while it rapidly decays in the former. Overlaid power laws of the form  $x^{-p}$  in the log plots to highlight decay rate,  $p$ .

The slightly smaller peak seen for the small domain DNS in comparison to the WRLES is consistent with the previously discussed higher speed-up values in the small domain case due to blockage effects. Higher speed flows around the cube naturally result in higher separation layer shear stress and increase turbulent production.

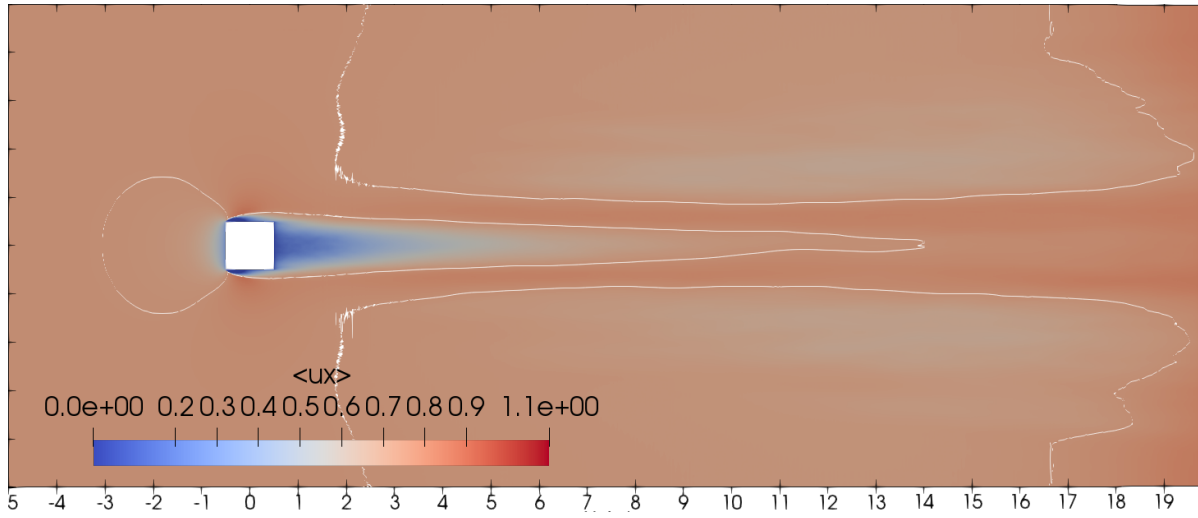
With the large domain for the WRLES cases we can examine the spanwise spreading as a function of distance from the cube (Fig. 18). For case D, the wake spreads with an angle of  $8^\circ$  and develops a region of slightly higher speed in the core of the wake after  $8h$ . The wake spread is very different for case C with a gradual contraction and two thin higher speed bands flanked by large lobes of reduced streamwise flow. The reason for these differences are apparent when examining the secondary flow patterns in the cross-streamwise planes (Fig. 19). The main horseshoe vortex for case A has grown to about  $0.5h$  by the end of the cube with a rotation such that high-speed fluid about the cube is convected down and towards the cube while low-speed near the ground is convected up and away from the cube. Thus, is the large horseshoe vortex which is responsible for high-speed bands in the cube wake for case C. A similar pattern is present for Case D but is much closer to the ground.

## 5 Summary

Though studied extensively, the case of the wall-mounted cube appears in many different engineering applications while efficient and accurate prediction of such flows remains elusive. Thus, there is a need for modeling improvements. However, simulation of experimental and field conditions is rather difficult if even possible. Therefore, there is also a need for simple datasets which can be used for model improvement studies. To this end, DNS of a wall-mounted cube at  $Re_h = 3900$  in a truncated domain with simplified boundary conditions have been performed. Two laminar inlet boundary layer profiles are considered, one with the cube immersed in the boundary layer and another with the boundary layer



(a) Case D:  $\delta_{99} = 0.25h$



(b) Case C:  $\delta_{99} = 2.0h$

Figure 18: Time-average velocity magnitudes at an elevation plane of  $y = 1$  for both Blassius inlet conditions at  $Re_h = 20K$ . Overlaid solid white line highlights full recovery of the inlet velocity at the cube height.

much smaller than the cube. The quality of the DNS has been evaluated in detail and used to guide WRLES resolution requirements to simulate a larger domain case at  $Re_h = 20K$ . We have shown the inlet profile to have a large effect on the general separation and wake structure with the standard recirculation bubble transitioning to a smaller cube-like region for the immersed case. Also for the immersed case, turbulence levels were predictably found to be significantly reduced primarily due to the reduced momentum traveling across the cube sides. Both bulk flow characteristics and wake turbulence have been shown to be  $Re$ -insensitive over the range examined. However, to examine far wake effects and because of the cost-savings afforded my LES, a larger domain was used for the WRLES. A small domain  $Re_h = 20K$  should be performed to allow direct comparison.

For a boundary layer thickness much smaller than the obstacle height, wake turbulence was found to decay rapidly like an axisymmetric wake. However, for the case of an obstacle immersed in the

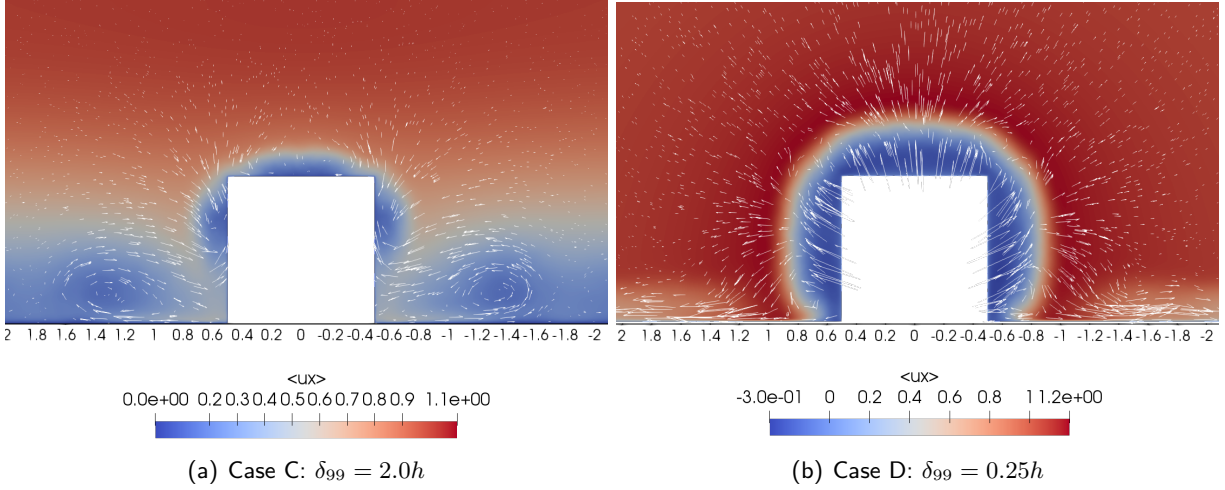


Figure 19: Time-average velocity streamwise velocity magnitude in the plane at the end of the cube at  $x = 0.5$  for both Blassius inlet conditions at  $Re_h = 20K$ . Overlaid in-plane vector field of cross-stream velocity field.

boundary layer, wake turbulence was found to decay much more gradually due to mean shear sustaining turbulent production. Analysis of near-cube production has led to both further evidence of a previously reported negative production mechanism for bluff-body flows and potential hazards of conflating unsteady structures with turbulence statistics as may be done in URANS for bluff-body flows. While the simple test conditions and small domain used here do not correspond to any real application, it is precisely their simplicity that makes their results useful for model development. The presented statistics may be used to evaluate and potentially improve RANS models, LES wall models, and guide LES resolution requirements.

From the DNS and WMLES performed here, we may draw some direct implications for the TAP project. As previously indicated by multiple sources in the literature,  $Re$ -scaling is a valid approach for predicting application-scale wind fields using wind tunnel and simulation results provided the model case is at least about  $Re_h \approx 4K$ . In particular, unless the turbine is taller than the obstacle, optimal placement downstream of an obstacle depends on the mean shear across the obstacle height. Though it will always be preferable to place a turbine above the obstacle height, mean shear may be beneficial when a turbine must be below the obstacle height due to increased turbulent mixing. Further, if there is very little mean shear present, placement of a turbine below the obstacle height and  $5h$  downstream is very nearly the same as placing the turbine above the obstacle height. However, these results are specific to a unit-obstacle. As discussed in the background section, high spanwise aspect ratio will shift this optimal placement to roughly  $20h$ . Thus, due to both sensitivity to mean velocity profiles and obstacle shapes, optimal turbine placement is highly site-specific.

## Acknowledgements

This project was funded by the U.S. Department of Energy (DOE) Energy Efficiency and Renewable Energy (EERE) WETO to Argonne under contract through DOE contract DE-AC02-06CH11357. Computing resources were provided by the Argonne Leadership Computing Facility, which is a DOE Office of Science User Facility supported under Contract DE-AC02-06CH11357. We are also grateful for the many discussions we have had with Prof. Ananias Tomboulides (University of Western Macedonia, Greece),

and Prof. Paul Fischer (University of Illinois at Urbana-Champaign, IL), which have contributed much to this study.

## References

- [1] B. Blocken, "LES over RANS in building simulation for outdoor and indoor applications: A foregone conclusion?," *Building Simulation*, vol. 11, pp. 821–870, 2018.
- [2] B. Blocken, "50 years of computational wind engineering: Past, present and future," *Journal of wind engineering and industrial Aerodynamics*, vol. 129, pp. 69–102, 2014.
- [3] A. Gosman, "Developments in cfd for industrial and environment applications in wind engineering," *Journal of Wind Engineering*, vol. 81, pp. 21–39, 1999.
- [4] S. Murakami, R. Ooka, R. Mochida, A. Yoshida, and S. Kim, "Cfd analysis of wind climate from human scale to urban scale," *Journal of Wind Engineering and Industrial Aerodynamics*, vol. 81, pp. 57–81, 1999.
- [5] R. Cowan, I. Castro, and A. Robins, "Numerical considerations for simulations of flow and dispersion around buildings," *Journal of Wind Engineering*, vol. 67, pp. 535–545, 2002.
- [6] I. Castro, H. Cheng, and R. Reynolds, "Turbulence over urban-type roughness: Deductions from wind-tunnel measurements," *Boundary-Layer Meteorology*, vol. 118, pp. 109–131, 2006.
- [7] S. R. Ahmed, G. Ramm, and G. Faltn, "Some salient features of the time -averaged ground vehicle wake," *SAE Transactions*, vol. 93, pp. 473–503, 1984.
- [8] K. Cooper, "Bluff-body aerodynamics as applied to vehicles," *Journal of Wind Engineering and Industrial Aerodynamics*, vol. 49, pp. 1–21, 1993.
- [9] Y. Wang, D. Thompson, and Z. Hu, "Effects of wall proximity on the flow over a cube and the implications for the noise emitted," *Physics of FLuids*, vol. 31, pp. 1–18, 2019.
- [10] P. Irwin, "Bluff body aerodynamics in wind engineering," *Journal of Wind Engineering and Industrial Aerodynamics*, vol. 96, pp. 701–712, 2008.
- [11] M. Tummers, M. Flikweert, K. Hanjalic, R. Rodink, and B. Moshfegh, "Impinging jet cooling of wall mounted cubes," *Proceedings of the ERCOFTAC International Symposium on Engineering Turbulence Modelling and Measurements*, pp. 773–782, 2005.
- [12] M. Popovac and K. Hanjalic, "Vortices and heat flux around a wall-mounted cube cooled simultaneously by a jet and a crossflow," *International Journal of heat and mass transfer*, vol. 52, pp. 4047–4062, 2009.
- [13] R. Wooding, E. Bradley, and J. Marshall, "Drag due to regular arrays of roughness elements of varying geometry," *Boundary-layer Meteorology*, vol. 5, pp. 285–308, 1972.
- [14] S. Leonardi and I. Castro, "Channel flow over large cube roughness: a direct numerical simulation study," *Journal of Fluid Mechanics*, vol. 651, pp. 519–539, 2010.
- [15] J. Claus, P. Krogstad, and I. Castro, "Some measurements of surface drag in urban-type boundary layers at various wind angles," *Boundary-Layer Meteorology*, vol. 145, pp. 407–422, 2012.

- [16] W. Anderson and C. Meneveau, "A large-eddy simulation model for boundary-layer flow over surfaces with horizontally resolved but vertically unresolved roughness elements," *Boundary-Layer Meteorology*, vol. 137, pp. 397–415, 2010.
- [17] Y. Jia, B. Sill, and T. Reinhold, "Effects of surface roughness element spacing on boundary-layer velocity profile parameters," *Journal of Wind Engineering*, vol. 73, pp. 215–230, 1998.
- [18] R. Macdonald, R. Griffiths, and D. Hall, "An improved method for the estimation of surface roughness of obstacle arrays," *Atmospheric Environment*, vol. 32, no. 11, pp. 1857–1864, 1998.
- [19] H. Cheng and I. Castro, "Near wall flow over urban-like roughness," *Boundary-Layer Meteorology*, vol. 104, pp. 229–259, 2002.
- [20] A. Yakhot, H. Liu, and N. Nikitin, "Free-surface instability correlations, and roughness-concentration effects on flow over hydrodynamically-rough surface," *USGS Water-Supply Paper 1592-C*, 1966.
- [21] R. Martinuzzi and C. Tropea, "The flow around surface-mounted, prismatic obstacles placed in a fully developed channel flow," *Journal of Fluids Engineering*, vol. 115, pp. 85–91, 1993.
- [22] E. Meinders, K. Hanjalic, and R. Martinuzzi, "Experimental study of the local convection heat transfer from a wall-mounted cube in turbulent channel flow," *Transactions of the ASME, Journal of Heat Transfer*, vol. 121, pp. 564–573, 1999.
- [23] A. Yakhot, H. Liu, and N. Nikitin, "Dns of turbulent flow around a wall mounted cube: A direct numerical simulation," *International Journal of heat and mass transfer*, vol. 27, pp. 994–1009, 2006.
- [24] W. Rodi, J. H. Ferziger, M. Breuer, and M. Pourquie, "Status of large eddy simulation: Results of a workshop," *Transactions of the ASME*, vol. 119, pp. 248–262, 1997.
- [25] H. Lim, T. Thomas, and I. Castro, "Flow around a cube in a turbulent boundary layer: Les and experiment," *Journal of Wind Engineering and Industrial Aerodynamics*, vol. 97, pp. 96–109, 2009.
- [26] T. Takahashi, S. Kato, S. Murakami, R. Ooka, M. Yassin, and R. Kono, "Wind tunnel tests of effects of atmospheric stability on turbulent flow over a three-dimensional hill," *Journal of Wind Engineering*, vol. 93, pp. 155–169, 2005.
- [27] J. Tomas and M. P. abd H. Jonker, "The influence of an obstacle on flow and pollutant dispersion in neutral and stable boundary layers," *Atmospheric Environment*, vol. 113, pp. 236–246, 2015.
- [28] S. Pospisil, S. Kuznetsov, H. Kozmar, and V. Michalcova, "Wind-tunnel simulation of thermally unstable atmospheric flow in complex terrain," *Structural and Physical Aspects of Construction Engineering*, vol. 190, pp. 575–580, 2017.
- [29] P. Hancock and P. Hayden, "Wind-tunnel simulation of weakly and moderately stable atmospheric boundary layers," *Boundary-Layer Meteorology*, vol. 168, pp. 29–57, 2018.
- [30] S. Pope, "A more general effective-viscosity hypothesis," *Journal of Fluid Mechanics*, vol. 72, no. 2, pp. 331–340, 1975.
- [31] P. Durbin, "Some recent developments in turbulence closure modeling," *Annual Review of Fluid Mechanics*, vol. 50, pp. 77–103, 2018.
- [32] I. Kimura and T. Hosoda, "A non-linear  $k$ - $\varepsilon$  model with realizability for prediction of flows around bluff bodies," *International Journal for Numerical Methods in Fluids*, vol. 42, pp. 813–837, 2003.

- [33] G. Park and P. Moin, "An improved dynamic non-equilibrium wall- model for large eddy simulation," *Physics of Fluids*, vol. 26, pp. 1–21, 2014.
- [34] U. Piomelli and E. Balaras, "Wall-layer models for large-eddy simulations," *Annual Review of Fluid Mechanics*, vol. 34, pp. 349–374, 2002.
- [35] G. Tabor and M. Baba-Ahmadi, "Inlet conditions for large eddy simulation," *Computers & Fluids*, vol. 39, pp. 553–567, 2010.
- [36] W. Schofield and E. Logan, "Turbulent shear flow over surface mounted obstacles," *Transactions of the ASME*, vol. 112, pp. 376–385, 1990.
- [37] I. Castro and A. Robins, "The flow around a surface-mounted cube in uniform and turbulent streams," *Journal of Fluid Mechanics*, vol. 79, pp. 307–335, 1977.
- [38] J. Hearst, G. Gomit, and B. Ganapathisubramani, "Effect of turbulence on the wake of a wall-mounted cube," *Transactions of the ASME*, vol. 804, pp. 513–560, 2016.
- [39] P. Saathoff and W. Melbourne, "Effects of free-stream turbulence on surface pressure fluctuations in a separation bubble," *Journal of Fluid Mechanics*, vol. 337, pp. 1–24, 1997.
- [40] W. Beranek and H. Korten, "Visual techniques for the determination of wind environment," *Journal of Wind Engineering and Industrial Aerodynamics*, vol. 43, pp. 205–306, 1979.
- [41] H. Woo, J. Peterka, and J. Cermak, "Wind tunnel measurements in wakes of structures," *NASA Technical Report Cr-2806*, 1976.
- [42] I. Castro, "Effects of free stream turbulence on low reynolds number boundary layers," *Journal of Fluids Engineering*, vol. 106, no. 3, pp. 298–306, 1984.
- [43] S. Murakami, R. Ooka, R. Mochida, A. Yoshida, and S. Kim, *Challenging Problems in Bluff Body Wakes*. Springer, Berlin, Heidelberg, 1993.
- [44] S. Depardon, J. Lasserre, J. Boueilh, L. Brizzi, and B. J., "Skin friction pattern analysis using near-wall piv," *Experiments in Fluids*, vol. 39, pp. 805–818, 2005.
- [45] K. Shah and J. Ferziger, "A fluid mechanics view of wind engineering: Large eddy simulation of flow past a cubic obstacle," *Journal of Wind Engineering and Industrial Aerodynamics*, vol. 67, pp. 211–224, 1997.
- [46] J. Smagorinsky, "General circulation experiments with the primitive equations. i. the basic experiment," *Mon. Weather Rev.*, vol. 91, pp. 99–164, 1963.
- [47] D. K. Lilly, "A proposed modification of the germano subgrid scale closure method," *Physics of Fluids A: Fluid Dynamics*, vol. 4, p. 633, 1992.
- [48] F. Nieuwstadt, P. Mason, C. Moeng, and U. Schumann, "Large eddy simulation of the convective boundary layer: a comparison of four computer codes," *Proceedings of the 8th Symposium on turbulent shear flows*, pp. 343–367, 1992.
- [49] B. E. Launder, G. J. Reece, and W. Rodi, "Progress in the development of a reynolds-stress turbulence closure," *Journal of Fluid Mechanics*, vol. 68, no. 3, pp. 537–566, 1975.
- [50] M. Kato and B. Launder, "The modeling of turbulent flow around stationary and vibrating square cylinders," *Proceedings of the 9th Symposium on turbulent shear flows*, vol. 115, pp. 10.4.1–10.4.6, 1993.

- [51] W. Rodi, "Experience with two-layer models combining the  $k$ - $\epsilon$  model with one-equation model near a wall," *AIAA Paper: 29th Aerospace Sciences Meeting*, vol. 91, 1991.
- [52] G. Ratnam and S. Vengadesan, "Performance of two equation turbulence models for prediction of flow and heat transfer over a wall mounted cube," *International Journal of Heat and Mass Transfer*, vol. 51, pp. 2834–2846, 2007.
- [53] J. Bredberg, S. Peng, and L. Davidson, "An improved  $k$ - $\omega$  turbulence model applied to recirculating flows," *International Journal of heat and mass transfer*, vol. 23, pp. 731–743, 2002.
- [54] A. Larousse, R. Martinuzzi, and C. Tropea, "Flow around surface-mounted, three-dimensional obstacles," *Turbulent Shear Flows*, vol. 8, pp. 127–139, 1993.
- [55] P. Durbin, "Separated flow computations with the  $k - \epsilon - \nu^2$  model," *AIAA Journal*, vol. 33, no. 4, pp. 659–664, 1995.
- [56] G. Iaccarino, C. Marongiu, P. Catalano, and M. Amato, "RANS simulation of the separated flow over a bump with active control," *Technical report, Center for Turbulence Research, Stanford University*, 2003.
- [57] J. Hwang and K. Yang, "Numerical study of vortical structures around a wall-mounted cubic obstacle in channel flow," *Physics of Fluids*, vol. 16, 2004.
- [58] C. Diaz-Daniel, S. Laizet, and J. Vassilicos, "Direct numerical simulations of a wall-attached cube immersed in laminar and turbulent boundary layers," *International Journal of heat and Fluid Flow*, vol. 68, pp. 269–289, 2017.
- [59] M. Saedi, P. LePoudre, and B. Wang, "Direct numerical simulation of turbulent wake behind a surface-mounted square cylinder," *Journal of Fluids and Structures*, vol. 51, pp. 20–39, 2014.
- [60] J. Bourgeois, P. Sattari, and R. Martinuzzi, "Alternating half-loop shedding in the turbulent wake of a finite surface-mounted square cylinder with a thin boundary layer," *Physics of Fluids*, vol. 23, pp. 1–15, 2011.
- [61] P. Sattari, J. Bourgeois, and R. Martinuzzi, "On the vortex dynamics in the wake of a finite surface-mounted square cylinder," *Experiments in Fluids*, vol. 52, pp. 1149–1167, 2011.
- [62] R. Vinuesa, P. Schlatter, J. Malm, C. Mavriplis, and D. Henningson, "Direct numerical simulations of the flow around a wall-mounted square cylinder under various inflow conditions," *Journal of Turbulence*, vol. 15, no. 6, pp. 555–587, 2015.
- [63] S. B. Pope, *Turbulent Flows*. Cambridge University Press, 2000.
- [64] J. Kim, D. Kim, and H. Choi, "An immersed-boundary finite-volume method for simulations of flow in complex geometries," *Journal of Computational Physics*, vol. 171, pp. 132–150, 2001.
- [65] C. Geuzaine and J. Remacle, "Gmsh: a three-dimensional finite element mesh generator with built-in pre- and post-processing facilities," *International Journal for Numerical Methods in Engineering*, vol. 79, no. 11, pp. 1309–1331, 2009.
- [66] P. Fischer, J. Lottes, and S. Kerkemeier, "NEK5000: An open source spectral element CFD solver," Available: [nek5000.mcs.anl.gov](http://nek5000.mcs.anl.gov), 2008.
- [67] J. Kim, P. Moin, and R. Moser, "Turbulence statistics in fully developed channel flow at low reynolds number," *Journal of Fluid Mechanics*, vol. 177, p. 133–166, 1987.

- [68] F. Nicoud and F. Ducros, "Subgrid-scale stress modelling based on the square of the velocity gradient tensor," *Flow, Turbulence and Combustion*, vol. 62, pp. 183–200, 1999.
- [69] A. Cimarella, A. Leonforte, E. D. Angelisa, A. Crivellini, and D. Angelini, "On negative turbulence production phenomena in the shear layer of separating and reattaching flows," *Physics Letters A*, vol. 383, no. 10, pp. 1019–1026, 2019.
- [70] P. Valente and J. Vassilicos, "The decay of turbulence generated by a class of multiscale grids," *Journal of Fluid Mechanics*, vol. 687, no. 25, pp. 200–340, 2011.
- [71] F. Frenkiel, "The decay of isotropic turbulence," *Journal of Applied Mechanics*, pp. 311–321, 1948.
- [72] P. Roach, "The generation of nearly isotropic turbulence by means of grids," *Heat and Fluid Flow*, pp. 82–92, 1986.



## **Computational Science Division**

Argonne National Laboratory  
9700 South Cass Avenue, Bldg. #240  
Argonne, IL 60439

[www.anl.gov](http://www.anl.gov)



U.S. DEPARTMENT OF  
**ENERGY**

Argonne National Laboratory is a U.S. Department of Energy  
laboratory managed by UChicago Argonne, LLC